

1 **Aseismic Fault Slip during a Shallow Normal-Faulting**
2 **Seismic Swarm Constrained Using a**
3 **Physically-Informed Geodetic Inversion Method**

4 **Yu Jiang¹, Sergey V. Samsonov², and Pablo J. González^{1,3}**

5 ¹COMET, Dept. Earth, Ocean and Ecological Sciences, School of Environmental Sciences, University of
6 Liverpool, Liverpool, L69 3BX, United Kingdom.

7 ²Canada centre for Mapping and Earth Observation, Natural Resources Canada, 560 Rochester Street,
8 Ottawa, ON K1S5K2, Canada.

9 ³Department of Life and Earth Sciences, Instituto de Productos Naturales y Agrobiología (IPNA-CSIC),
10 38206 La Laguna, Tenerife, Canary Islands, Spain.

11 **Key Points:**

- 12 • We estimate time-dependent fault slip to interpret geodetic data by applying a
13 low dimensional model for elliptical slip distributions.
- 14 • Significant aseismic slip during the initial stage preceded the most energetic event
15 M4.6 in the 2011 Hawthorne shallow seismic swarm.
- 16 • Lower bounds of average slip rate are similar to other slow-slip phenomena, im-
17 plying aseismic processes might play a notable role in swarms.

Corresponding author: Yu Jiang, jiangyuinsar@gmail.com

18 **Abstract**

19 Improved imaging of the spatio-temporal growth of fault slip is crucial for understand-
20 ing the driving mechanisms of earthquakes and faulting. This is especially critical to prop-
21 erly evaluate the evolution of seismic swarms and earthquake precursory phenomena. Fault
22 slip inversion is an ill-posed problem and hence regularisation is required to obtain sta-
23 ble and interpretable solutions. An analysis of compiled finite fault slip models shows
24 that slip distributions can be approximated with a generic elliptical shape, particularly
25 well for $M \leq 7.5$ events. Therefore, we introduce a new physically-informed regularisation
26 to constrain the spatial pattern of slip distribution. Our approach adapts a crack model
27 derived from mechanical laboratory experiments and allows for complex slipping pat-
28 terns by stacking multiple cracks. The new inversion method successfully recovered dif-
29 ferent simulated time-dependent patterns of slip propagation, i.e., crack-like and pulse-
30 like ruptures, directly using wrapped satellite radar interferometry (InSAR) phase ob-
31 servations. We find that the new method reduces model parameter space, and favours
32 simpler interpretable spatio-temporal fault slip distributions. We apply the proposed method
33 to the 2011 March-September normal-faulting seismic swarm at Hawthorne (Nevada, USA),
34 by computing ENVISAT and RADARSAT-2 interferograms to estimate the spatio-temporal
35 evolution of fault slip distribution. The results show that (1) aseismic slip might play
36 a significant role during the initial stage, and (2) this shallow seismic swarm had slip rates
37 consistent with those of slow earthquake processes. The proposed method will be use-
38 ful in retrieving time-dependent fault slip evolution and is expected to be widely appli-
39 cable to studying fault mechanics, particularly in slow earthquakes.

Plain Language Summary

41 A key earthquake science challenge is to understand when an instability on a fault
42 will arrest or run away into a large rupture. However, the slip nucleation process seems
43 not to produce seismic waves and hence remains hidden to most seismological methods.
44 Geodetic methods, which can directly measure motions at earth's surface, offer a com-
45plementary tool to improve our ability to map the fault slip. In this work, we expand
46an experimentally observed crack model, and propose a new inversion method for find-
47ing models of fault slip that can fit the observations of surface motions. The new method
48greatly reduces computation complexity respecting previous state-of-the-art methods,
49and is validated against synthetic experiments. We apply this new method to 2011 Hawthorne
50earthquake swarm (Nevada, USA), and discovered an aseismic slow slip before seismic-
51ity rate increased. That preparation stage was followed by a triggered larger slip on a
52nearby fault, and after that, the seismicity and fault slip rate reduced rapidly. We ex-
53pect that this new methodology will be applied to detect similar precursory aseismic slip
54during long-lasting earthquake sequences, and allow us to retrieve detailed slip growth
55in space and time, which ultimately will advance our understanding of the faulting me-
56chanics.

1 Introduction

How fault slip nucleates, grows and eventually accelerates is a critical question to describe the driving mechanisms behind earthquakes and faulting phenomena. Our current understanding is consistent but cannot distinguish among various viable mechanisms to explain how fault slip initiates: dynamic triggering (Gomberg & Johnson, 2005), tidal triggering (Delorey et al., 2017), pore-pressure diffusion (Parotidis et al., 2003) or aseismic slip (Radiguet et al., 2016; Gualandi et al., 2017; Caballero et al., 2021). In particular, Gomberg (2018) summarised two leading hypotheses for earthquake nucleation. Ranging from a stochastic model in which each earthquake triggers subsequent ones in a cascade fashion, to an alternative that favours a deterministic view where slow-slip triggers and/or precedes the occurrence of a seismically dynamic rupture. Within the scope of increasing our capacity to distinguish between the earthquake nucleation models, a promising venue is to increase our ability to image how fault slip evolves in space and time. Although fault slip evolution is not necessarily the only cause of seismicity migrating, improvements in this direction may provide crucial data to examine hypotheses for earthquake nucleation mechanisms.

Fault slip imaging improvements are particularly desirable to estimate (seismic and aseismic) slip propagation parameters, such as slip rate, and gain deeper insights into the physics controlling regular earthquakes and slow-slip phenomena. Regular earthquakes are known to show peak and average slip rates of the order of 1 m/s and 0.1 m/s (Takenaka & Fujii, 2008). While slow-slip phenomena show much lower slip rates, e.g., Slow Slip Events (SSEs), fault creep, or slip related to fluid injection. For example, in the case of SSEs in subduction zones, the peak slip rates vary around 0.1~3 cm/day (Radiguet et al., 2011; Bletery & Nocquet, 2020; Rousset et al., 2019; Ozawa et al., 2019). In the case of the episodic creep event, the slip rates in continental faults are 0.5~3 cm/year (Schmidt et al., 2005; Jolivet et al., 2012; Hussain et al., 2016; Scott et al., 2020). In fluid injection experiments, the slip rates have been observed to be much higher, up to 4×10^{-3} mm/s (35 cm/day) (Guglielmi et al., 2015).

Hence, to evaluate (seismic and aseismic) fault slip characteristics, a better description of how fault slip propagates in space and time is necessary. Including complex propagation patterns of fault slip such as pulse-like and crack-like ruptures (Lambert et al., 2021; Marone & Richardson, 2006). Such patterns have been observed during regular

89 earthquakes but are also associated with slow-slip phenomena: with slow slip transients
90 migrating further away from where they started along strike (or dip), or remain station-
91 ary through time. Observations of some SSEs and "Episodic Tremor and Slip" (ETS)
92 show pulse-like rupture characteristics with elongated slipping areas, e.g., the Cascadia
93 subduction zone (Michel et al., 2019), and with along strike migration speeds of ~ 10 km/day
94 (Wech et al., 2009; Rousset et al., 2019). In contrast, slip propagation of meter-scale fluid
95 injection experiments indicates stationary patterns: Bhattacharya and Viesca (2019) pro-
96 posed a model in which the slip grows as an expanding ellipse, with the injection point
97 as the slipping centre. The latter phenomenon is also found in some SSEs on subduc-
98 tion zones, e.g., the deep Manawatu and Kaimanawa SSEs on the Hikurangi subduction
99 zone (Wallace, 2020). Here, we aim to improve fault slip mapping in space and time to
100 contribute to the advancement of the study of fault slip processes using, yet underutilised,
101 satellite InSAR observations.

102 In this research, we developed a new method to interpret directly wrapped phase
103 InSAR observations to estimate the spatio-temporal fault slip, in particular, in the con-
104 text of a favourable tectonic setting, continental seismic swarms (e.g., small-amplitude
105 surface deformation signals and/or phase discontinuities due to surface ruptures). In-
106 SAR has been used to map surface displacements with high spatial resolution and sub-
107 sequently model fault slip. But so far, it is more common to estimate static slip distri-
108 butions than jointly invert for the time-series of slip evolution (Floyd et al., 2016; Ingleby
109 et al., 2020). The problem of retrieving time series of source parameters from non-simultaneous
110 and temporally overlapped multi-sensor observations is ill-posed; however, the oscilla-
111 tions of the solution caused by the rank deficiency of this problem can be reduced by ap-
112 plying regularisation or temporal filtering (Samsonov & D'Oreye, 2012). Grandin et al.
113 (2010) introduced a temporal smoothing scheme as an additional constraint to retrieve
114 the time series of magma volume changes. Additionally, González et al. (2013) used trun-
115 cated singular value decomposition (TSVD) to reject model space basis vectors associ-
116 ated with small singular values. Instead of regularising the volume variation itself, they
117 minimised the volume change rate, to avoid large discontinuities. Here, we improve pre-
118 vious methods by a) regularising the fault slip distribution using a prescribed param-
119 eterisation derived from a laboratory-based crack model, and b) introducing a statisti-
120 cally optimal truncation criterion that allows to automatically separate signal and noise
121 in the spatio-temporal fault slip distributions. We demonstrated the validity of this ap-

122 proach using synthetic experiments and comparing it against a compilation of published
123 slip distribution models. Finally, we applied the new proposed methodology to the 2011
124 Hawthorne seismic swarm (Nevada, USA). The 2011 Hawthorne seismic swarm is located
125 at the central Walker Lane, which accommodates the Pacific-North American transform
126 plate motion by oblique-normal faults and block rotations. The 2011 Hawthorne swarm
127 consists of 10 M4+ events, and the largest earthquake among them is an M4.6 event (Zha
128 et al., 2019; Smith et al., 2011); a recent study using satellite images reveals clear sur-
129 face deformation signals before the M4.6 event, and the geodetic moment is much higher
130 than the seismic moment, indicating that aseismic slip dominates the fault behaviour (Jiang
131 & González, 2021). By applying our proposed methodology, we retrieved the fault-slip
132 spatio-temporal evolution, and explored the interactions between the fault slip and the
133 seismicity.

134 **2 Time-Dependent Fault Slip Inferred Using Geodetic Fault Slip Mod-** 135 **els**

136 **2.1 Static Fault Slip Models**

137 Slip inversions with kinematic models are ill-posed problems in which the solution
138 is nonunique and unstable, and unphysical slip distributions can be estimated by least-
139 squares algorithms, i.e., extremely rough oscillatory slip distributions. Harris and Segall
140 (1987) introduced Laplacian smoothing as the regularisation scheme. This minimises the
141 second derivative of slip and can prevent cases with large stress drops. Du et al. (1992)
142 plotted a trade-off curve for misfit as a function of slip roughness, and manually picked
143 a smoothing factor within the inflection point of the curve to find an optimal balance
144 between data fit and model roughness. Matthews and Segall (1993) determined the op-
145 timal smoothing factor in the trade-off curve objectively by implementing the cross-validation
146 method. Much later, Fukahata and Wright (2008) and Fukuda and Johnson (2008) in-
147 troduced the Bayesian approach, ABIC (Akaike’s Bayesian Information Criterion), to
148 solve the slip distribution. While Fukahata and Wright (2008) emphasised the signifi-
149 cance of fault geometry as a nonlinear constraint, Fukuda and Johnson (2008) overcame
150 the deficiencies of ABIC with positivity constraints, and then applied the adapted ABIC
151 to simultaneously estimate the slip distribution and smoothing parameter objectively in
152 a Bayesian framework. Fukuda and Johnson (2010) then devised a mixed linear-non-linear
153 Bayesian inverse formulation and extended their work for the joint slip and geometry in-

154 version. In response, Minson et al. (2013) argued that the non-physical regularisation
155 scheme (i.e., Laplacian smoothing) is unnecessary, and developed a fully Bayesian ap-
156 proach to sample all possible families of models compatible with the observations, via
157 a parallel computing framework. Ragon et al. (2018) further extended the work of Minson
158 et al. (2013) and accounted for the uncertainty in fault geometry. Instead of Laplacian
159 regularisation, Amey et al. (2018) developed an inversion package *slipBERI*, and incor-
160 porated self-similarity, characterising the seismic slip distribution in real earthquakes,
161 as a prior assumption within the Bayesian inversion of earthquake slip.

162 All the previous methods are based on kinematic models that do not take into ac-
163 count the relationship between stress and slip in the fault. Alternatively, dynamic source
164 models satisfy physical constraints on the propagation of shear fractures on Earth, but
165 few dynamic source models are considered to constrain the slip inversions. As an alter-
166 native, Di Carli et al. (2010) proposed using elliptical patches to describe the slip dis-
167 tribution in the kinematic and dynamic inversion of near-field strong motion data at low
168 frequencies. Soon afterwards, Sun et al. (2011) put forward a *mechanical* slip inversion,
169 imposing a uniform stress drop on the fault plane. The resulting slip distribution is in-
170 herently smooth, so the smoothing norm and the smoothing factor are unnecessary. Tridon
171 et al. (2016) assumed a circular stress patch in volcano research, inverting the displace-
172 ment for shear and normal stresses simultaneously, along with the fault geometry.

173 In this study, we apply a new methodology named Geodetic fault-slip Inversion us-
174 ing a physics-based Crack Model (GICMo) (Jiang et al., 2022). In this method, we take
175 advantage of a one-dimensional analytical crack model proposed by Ke et al. (2020). The
176 model was theoretically and experimentally validated in self-contained ruptures within
177 a 3-meter-long saw-cut granite fault. This new crack model features non-singular (finite)
178 peak stresses at the rupture tip. In Jiang et al. (2022), we expanded the one-dimensional
179 model into two dimensions to produce elliptical fault slip shapes/patches. We assume
180 that one of the focal points of the ellipse is the crack centre (with the maximum slip)
181 and the elliptical perimeter to be the crack tip. Therefore, the slip distribution on the
182 fault plane is controlled by a very compact and reduced set of parameters. The geodetic-
183 inverted fault slip infers that it is possible that the crack centre can be located at the
184 rupture centre, e.g., the 2009 L'Aquila earthquake (Walters et al., 2009). To adapt to
185 this possibility, we relax the constraint that the maximum slip should coincide with the
186 crack centre location, and allow it to move along the x axis inside the ellipse. Hence, our

187 crack model contains only eight parameters as demonstrated by Equation 1 and Figure 1.

$$s = \mathbf{f}(x_0, y_0, a, e, \alpha, \lambda, d_{max}, \theta) \quad (1)$$

188 where s is the slip distribution; x_0, y_0 are the locations of the crack centre ; a and e are
 189 the semi-major axis and eccentricity of the ellipse; α is the ratio controlling the location
 190 of the crack centre along x axis: the crack centre is located at the ellipse centre , left/right
 191 vertices when $\alpha = 0, -1/1$; λ is the ratio controlling the displacement transition from
 192 the centre to the edge of the elliptical crack; d_{max} is the maximum slip; θ is the rake an-
 193 gle.

194 In the GICMo method, once the crack model parameters are provided, the slips
 195 for all fault patches are then determined based on the two-dimensional crack model dis-
 196 cussed above. Then, the fault slip distribution is forward modelled to estimate surface
 197 displacement. Following Jiang and González (2020), a misfit function is constructed based
 198 on the wrapped phase residuals and the weighting matrix. The misfit function is then
 199 regarded as the likelihood function fed into the Bayesian process to retrieve the poste-
 200 rior distribution of crack model parameters. In the Bayesian process, the Markov chain
 201 Monte Carlo algorithm is adopted as the probability sampling approach based on the
 202 Metropolis-Hasting rule.

203 Here we design a synthetic static slip to compare the performance of our method,
 204 GICMo, and a state-of-the-art method, slipBERI (Amey et al., 2018). The geodetic in-
 205 version package, slipBERI, solves for fault slip with GNSS and unwrapped InSAR phases
 206 in a Bayesian approach using von Karman regularisation, and simultaneously solves for
 207 a hyperparameter that controls the degree of regularisation. A normal fault with pure
 208 down-dip slip is simulated as the synthetic fault model. To imitate the slipping patterns
 209 observed in the published finite-source rupture models SRCMOD (Mai & Thingbaijam,
 210 2014) (e.g., Bennett et al. (1995), Ichinose et al. (2003), and Elliott et al. (2010)), the
 211 inner region is a square area with a larger displacement, and the outer region is an an-
 212 nulus area with a smaller displacement (Figure 2). Due to the difference in the inges-
 213 tion data, the synthetic phases are unwrapped phases for slipBERI and wrapped phases
 214 for GICMo. The displacement phase is forward calculated based on the synthetic fault
 215 slip distribution and the dislocation model. To increase its resemblance to reality, decor-
 216 relation and atmosphere noises are simulated and added, whose amplitudes are 10% of
 217 2π for wrapped phase cases or the peak amplitude of the deformation phase for unwrapped

218 phase cases, which is based on the signal-to-noise ratio from a real interferogram in Sec-
 219 tion 4 (RS2-20110322-20110415). The simulated noise-plus-deformation interferogram
 220 is resampled with a quadtree algorithm within the downsampled unwrapped and wrapped
 221 phases (Bagnardi & Hooper, 2018; Jiang & González, 2020). In addition, the covariance
 222 matrix is estimated based on the phase in the far-field. Finally, the downsampled phases
 223 and covariance matrix are fed into slipBERI and GICMo to retrieve the slip distribu-
 224 tions. Figures 2b-2d show the modelled slip distribution inverted by GICMo and slip-
 225 BERI, and Figure S1 shows the modelled phase and phase residuals. The conclusions
 226 are listed below.

227 (1) Both GICMo and slipBERI provide the first-order accuracy of the slip distri-
 228 bution, including the locations of the crack centre and the magnitude of the slip peak.

229 (2) We interpolate the slip distribution onto a $0.5 \text{ km} \times 0.5 \text{ km}$ patch mesh, and
 230 calculate the root-mean-square error (RMSE) of the slip distribution compared with the
 231 synthetic slip distribution. We find that the RMSEs are 1.5 cm for the one-ellipse model,
 232 2 cm for the von Karman smoothing model, and 3 cm for the Laplacian smoothing model,
 233 which are approximately similar. However, the great advantage is that the parameters
 234 to be solved in GICMo are independent of the fault mesh discretization, and the num-
 235 ber of parameters is 30 times less in this case than 201 in slipBERI for this case.

236 **2.2 Bayesian Inversion of Fault Slip Time-Series Using a Physics-based** 237 **Crack Model (Time-GICMo)**

238 The temporal evolution of fault slip is critical to understanding the driving mech-
 239 anism of slow slip. It is difficult to find one slow slip event where one interferogram can
 240 coincidentally capture the beginning and the ending of the activity. Instead, a common
 241 scenario is that the slip increment is captured by interferograms. In this section, we de-
 242 velop a new method of retrieving the slip increments and demonstrate the time-series
 243 slip estimation with synthetic experiments. Assuming two elliptical ruptures at the be-
 244 ginning and the ending, slip increment $\Delta s = s^2 - s^1$, where s^2 and s^1 are the slip dis-
 245 tributions at the end and the beginning of the interferogram.

246 We consider a system of N increments of fault slip ($\Delta s^n \in [\Delta s^1, \dots, \Delta s^N]$) between
 247 dates t_i^n and t_j^n) based on the non-linear inversion estimation from the corresponding wrapped
 248 interferogram, and the raw images of interferograms are acquired at M unique dates ($t \in$
 249 $[t_1, \dots, t_M]$). The aim is to solve for the temporal evolution of fault slips ($s \in [s_1, \dots, s_M]$)

250 for each date. We assume that the slip rate between adjacent dates ($v_m \in [v_1, \dots, v_{M-1}]$)
 251 is constant, so the slip increment Δs^n can be expressed by the sum of fault slip incre-
 252 ment between adjacent dates, $\Delta s^n = \sum_{m=i}^{j-1} v_m (t_{m+1}^n - t_m^n)$. The linear expression for
 253 N increments of fault slip is shown in Equation 2, as illustrated by González et al. (2013):

$$\begin{aligned} \mathbf{P} &= \mathbf{B}\mathbf{Q} \\ \mathbf{P} &= [\Delta s^1 \quad \dots \quad \Delta s^n \quad \dots \quad \Delta s^N]^T \\ \mathbf{Q} &= [v_1 \quad \dots \quad v_m \quad \dots \quad v_{M-1}]^T \\ \mathbf{B}(n, m) &= \begin{cases} t_{m+1}^n - t_m^n, & \text{if } i \leq m \leq j - 1. \\ 0, & \text{otherwise.} \end{cases} \end{aligned} \quad (2)$$

254 where \mathbf{P} is the observation vector, \mathbf{Q} is the unknown vector, and \mathbf{B} is the designed ma-
 255 trix. Considering there are N increments of fault slip, the matrix dimension is $(N \times 1)$
 256 for \mathbf{P} , $(N \times (M - 1))$ for \mathbf{B} , and $((M - 1) \times 1)$ for \mathbf{Q} . Then, we decompose matrix \mathbf{B}
 257 by using the SVD methods,

$$\mathbf{B} = \mathbf{U}\mathbf{S}\mathbf{V}^T \quad (3)$$

258 where \mathbf{U} is an orthogonal matrix with columns that are the basis vectors of the data space
 259 $(N \times N)$, \mathbf{V} is an orthogonal matrix with columns that are the basis vectors spanning
 260 the singular values of the model $((M - 1) \times (M - 1))$, and \mathbf{S} is a diagonal matrix of
 261 the singular values $((N \times (M - 1)) \times 1)$. A solution for this problem can be obtained
 262 as follows,

$$\mathbf{Q} = \mathbf{V}\mathbf{S}^{-1}\mathbf{U}^T\mathbf{P} \quad (4)$$

263 If $\text{rank}(\mathbf{B}) < m$, the solution obtained using the SVD technique may contain numerical
 264 instabilities when there are small singular values. In this case, a more stable solution can
 265 be achieved using the TSVD method (Aster et al., 2019), which rejects model space ba-
 266 sis vectors associated with small singular values, up to a certain threshold. As an im-
 267 provement upon González et al. (2013), we apply an optimal hard threshold for singu-
 268 lar values truncation proposed by Gavish and Donoho (2014). Gavish and Donoho (2014)
 269 proposed that the optimal hard threshold for singular value is $4/\sqrt{3}$ of the median sin-
 270 gular value. This criterion is empirically proven to be the best hard thresholding, inde-
 271 pendent of model size, noise level, or true rank of the low-rank model. This improvement

272 allows us to define the degree of regularisation based on an objective criterion, which gener-
 273 erates a parsimonious low-rank model solution in the presence of noisy data. Note that
 274 in order to retrieve a realistic solution, a non-negative constraint is added in solving for
 275 slip rate vector Q implemented by using MATLAB function *lsqnonneg* ([https://uk.mathworks](https://uk.mathworks.com/help/optim/ug/lsqnonneg.html)
 276 [.com/help/optim/ug/lsqnonneg.html](https://uk.mathworks.com/help/optim/ug/lsqnonneg.html)). It is physically appropriate because slip along
 277 faults rarely re-rupture backwards (Hicks et al., 2020).

278 **3 Time-dependent Fault Slip Inversion Experiments**

279 In this section, we describe two experiments to investigate if this method can re-
 280 trieve pulse- and crack-like rupture propagation patterns in space and time. We tested
 281 the performance of the inversion method to recover fault slip evolution from each of the
 282 two-ellipse models.

283 The first synthetic case aims to explore the inversion with overlapping ruptures (Fig-
 284 ure 3). Several recent studies have suggested spatial overlap between coseismic slip and
 285 afterslip (Barnhart et al., 2016; Bedford et al., 2013; Bürgmann et al., 2002; Johnson et
 286 al., 2012; Pritchard & Simons, 2006; Salman et al., 2017; Tsang et al., 2016). A series
 287 of overlapping elliptical cracks are simulated in Figure 3a, and a forward inversion is per-
 288 formed to calculate the surface displacement due to the slip increment between adjacent
 289 cracks. We aimed to compare the results based on various geodetic inversion algorithms:
 290 (1) the one-ellipse model, as described in Section 2.1, (2) a von Karman regularisation
 291 algorithm (Amey et al., 2018), (3) the two-ellipse model with different crack centres.
 292 Inversion results are shown in Figures 3b-3d, and the modelled phase and residuals are
 293 shown in Figures S2-S3. The main conclusions are as follows.

294 (1) The RMSEs of the fault slip residual is the lowest in results based on the two-
 295 ellipse model with different centres. The triangle patch size in the crack model is ~ 0.84 km,
 296 and the rectangle patch size in slipBERI is 1.5 km. In this way, we interpolated the mod-
 297 elled slip distributions to grid points with 1.17 km spacing, and then calculated the RMSE
 298 of the fault slip residual. In each case, the RMSE of slip residuals based on the two-ellipse
 299 model with different centres (Figure 3d) are the smallest, and the average RMSE for the
 300 one-ellipse model, the von Karman smoothing model and the two-ellipse model are 0.9 cm,
 301 1.6 cm, and 0.6 cm.

302 (2) The two-ellipse model is superior to the one-ellipse model in the F-test for the
 303 residual of the interferometric phase. The two-ellipse model has more free parameters,

304 leading to an inherent improvement in the data fit. To objectively compare the model
 305 performances, we use the F-ratio statistic to test the significance of the decrease of resid-
 306 uals between models (Stein & Gordon, 1984). The statistical test checks if the empir-
 307 ical F-ratio (F_{emp}) is larger than the theoretical (F_{theory}). In this case, the comparison
 308 of the one-ellipse model and two-ellipse model leads to $F_{emp} = 72.8 \gg F_{theory} = 2.6$.

309 The second synthetic case aims to explore the inversion with the containing rup-
 310 tures (Figure 4). A growing rupture has been widely observed and studied in fluid in-
 311 jection experiments (Guglielmi et al., 2015; Bhattacharya & Viesca, 2019; Cappa et al.,
 312 2019). The rupture centre is located at the injection point, and the radius of the slip-
 313 ping zone grows at a rate up to 10^{-6} m/s. A set containing elliptical ruptures is sim-
 314 ulated in Figure 4a, and a forward inversion facilitates the surface displacement calcu-
 315 lation. We aimed to retrieve the slip increments from the observed interferometric phase
 316 with various methods described above (one-ellipse model, von Karman smoothing model,
 317 and two-ellipse model). On noticing that the slip distribution is not well resolved by the
 318 two-ellipse model with different centre s , we added another constraint to the two-ellipse
 319 model so that both cracks share the same centre s . The inversion results are shown in Fig-
 320 ures 4b-4e, and the modelled phase and residuals are shown in Figures S4-S5. The main
 321 conclusions are as follows.

322 (1) The average RMSE of slip residuals based on various inversion models (one-
 323 ellipse model, von Karman smoothing model, two-ellipse model with different centre s ,
 324 and one centre s) are 1.3 cm, 1.3 cm, 1.0 cm, and 0.8 cm. The one-ellipse model failed
 325 because the slip increment in containing ruptures no longer could be described by one
 326 complete crack. Indeed, slipBERI showed better performance because it inferred the re-
 327 gion with the slip peak. The two-ellipse model with different centres is even better but
 328 was not well resolved, e.g., the slip increment from t_1 to t_2 (second image in Figure 4c).
 329 Therefore, the two-ellipse model with the *same* centre is the most appropriate for recon-
 330 structing the cracks' locations, sizes, and maximum slips.

331 (2) In the F-test of the interferometric phase residuals, the two-ellipse model with
 332 the same centre is superior to the two-ellipse model with different centre s , and the one-
 333 ellipse model is the least useful.

4 Application case: the 2011 Hawthorne Seismic Swarm (Nevada, USA)

4.1 Regional Tectonics and Seismicity

We apply our algorithm to the 2011 Hawthorne seismic swarm, which occurred on the central Walker Lane (Figure 5). The Walker Lane is a 500 km-long and 100 km-wide deformation region consisting of N-NW right-lateral shear and extension (Wesnousky, 2005). It is located between the northwest translating Sierra Nevada microplate and the westward extending Basin and Range Province. The Walker Lane accommodates 20% \sim 25% of the current relative motion (50 mm/year) between the Pacific and North American plates (Argus & Gordon, 1991; Faults & Henry, 2008). The central Walker Lane accommodates the deformation budget of \sim 8 mm/year between the Basin and Range province and the central Sierra Nevada (Bormann et al., 2016). The distributed dextral shear in central Walker Lane is accommodated by oblique-normal faults, block rotations, and partitioning of oblique deformation between sub-parallel normal and strike-slip faults. The total long-term strain rate is 51 nanostrain/year extension directed N77°W and 38 nanostrain/year contraction directed N13°E (Kreemer et al., 2014), much higher than the central Basin and Range (Kreemer et al., 2009).

Being a geologically young and developing fault system, the Walker Lane shows high levels of seismicity over the instrument period, including >10 M6+ earthquakes in the last century. Since 2000, the Walker Lane was struck by a few seismic sequences with some accompanied by aseismic slip evidence. For example, for the 2008 Mogul earthquake sequence, geodetic observation and modelling indicated significant aseismic slip (Bell et al., 2012), and the migration speed of the largest foreshock cluster is consistent with aseismic slip (Ruhl et al., 2016); for the 2014 Virginia City Swarm migration rate of small earthquakes was consistent with rates observed elsewhere associated with pore fluid diffusion and aseismic creep (Hatch et al., 2020). However, there was no clear indication of aseismic slip during the 2016 Nine Mile Ranch sequence (Hatch-Ibarra et al., 2022), the 2017 Truckee sequence (Hatch et al., 2018) or the 2020 Monte Cristo Range sequence (Ruhl et al., 2021).

The 2011 Hawthorne seismic swarm lasted from March to September and consisted of 10 M4+ earthquakes according to the U.S. Geological Survey (USGS) hypocentre catalogue (<https://earthquake.usgs.gov/earthquakes/search/>). This sequence occurred in the footwall block of the Wassuk Range segment at the central Walker Lane (Faults

366 & Henry, 2008), and this segment experiences a significant extension of 1.5 ± 0.3 mm/year
367 (Hammond & Thatcher, 2007). Early moment tensor solutions show the shallow depths
368 in this sequence (Smith et al., 2011), and further hypocentre relocation together with
369 the focal mechanisms of the M4+ events consistently reveal a W-NW-dipping normal
370 fault zone with centroid depths between 2 km and 4 km (Zha et al., 2019). The 2011 Hawthorne
371 sequence is close to the Aurora-Bodie volcano (Lange & Carmichael, 1996), but no vol-
372 canic signature was observed in near-source seismograms, which infers this sequence is
373 not likely related to the magmatic activity (Smith et al., 2011; Zha et al., 2019). In this
374 research, we were able to identify three stages with respect to the timing of the most en-
375 ergetic event (M4.6) occurred: an initial stage (pre-M4.6 stage) from 15 March to 17 April,
376 a shorter period around the most energetic stage (co-M4.6 stage), and the post-energetic
377 stage (post-M4.6 stage) lasting until 17 September.

378 **4.2 Multi-satellite Geodetic Datasets**

379 We processed ENVISAT and RADARSAT-2 data and generated 8 SAR interfer-
380 ograms to quantify surface displacements (Figure 6). SAR images were acquired between
381 February and September 2011 from two tracks: one ascending track from the Canadian
382 Space Agency RADARSAT-2 satellite, look angle of 35° and heading angle of 350° ; and
383 another descending track from the European Space Agency (ESA) ENVISAT satellite,
384 track 343, look angle of 35° and heading angle of -166° . Interferograms were processed
385 in two-pass differential mode, using a 30 m resolution digital elevation model (DEM) de-
386 rived from the Shuttle Radar Topography Mission. ENVISAT-ASAR data were processed
387 using Doris software (Kampes et al., 2003) and ISCE software, RADARSAT-2 data us-
388 ing GAMMA software (Werner, 2000). Overall, we obtained 8 short baseline differen-
389 tial interferograms. The computed interferograms have temporal separations ranging from
390 24 to 120 days. Considering the dominant extensional mechanism and N-S fault strik-
391 ing in this region, the preferred movement direction of the ground displacement is E-W.
392 Consequently, the satellite flight direction favours surface displacement observations in
393 this normal faulting system.

394 Interestingly, 2 ascending RADARSAT-2 interferograms during the pre-M4.6 stage
395 indicated clear surface displacement signals (Figure 6d and 6a), ~ 4 cm away from satel-
396 lite line-of-sight motion. In interferograms covering the co-M4.6 stage, it is notable that
397 surface displacement signals were larger in magnitude and located further north with re-

398 spect to the pre-M4.6 stage (Figures 6b, 6c, 6e and 6f). During the early post-M4.6 stage,
 399 surface displacements were detected along a very narrow spatial band with clear phase
 400 discontinuities, suggesting surface ruptures (Figure 6g). For one interferogram covering
 401 the late post-M4.6 stage (Figure 6h), the phase was dominated by atmospheric noise and
 402 no clear deformation signal was detected. Analysis of interferograms suggests that fault
 403 slip may have occurred along a fault system with a two-plane geometry, which is con-
 404 sistent with the finding from early moment tensor solutions (Smith et al., 2011).

405 Note that the 2 ascending RADARSAT-2 interferograms provide a unique oppor-
 406 tunity to look into the preseismic slip, which is not available in other reported cases due
 407 to the data limitation. For example, for the 2008 Mogul earthquake swarm, Bell et al.
 408 (2012) measured the surface deformation covering the whole earthquake swarm using In-
 409 SAR and they found that the modelled cumulative geodetic moment is ~ 2 times the cu-
 410 mulative seismic moment, indicating a significant portion of aseismic slip. However, they
 411 cannot separate the preseismic deformation signal because there is no available interfer-
 412 ogram covering the preseismic stage only. In addition, the GPS observations covering
 413 the 2008 Mogul earthquake swarm cannot constrain the preseismic slip well due to the
 414 low signal to noise ratio in GPS solutions (Ruhl et al., 2016).

415 **4.3 Spatio-temporal Slip Evolution**

416 To develop the kinematic fault model, we first constructed the fault geometry de-
 417 rived from a non-linear fault inversion of InSAR wrapped phase observations, solving for
 418 uniform distribution on rectangular faults (Jiang & González, 2020). A geodetic inver-
 419 sion directly using the interferometric wrapped phase avoids any potential phase unwrap-
 420 ping error (Figure S6). The data variance-covariances describing the noise level are cal-
 421 culated based on the covariograms (Figure S7) and are used to weight the wrapped phase
 422 residuals in the likelihood function as illustrated by Jiang and González (2020). Mod-
 423 elling of a selection of interferograms covering the successive phases confirmed that ground
 424 motion could be caused by fault geometry with two distinct planes. During the pre-M4.6
 425 stage, the observed ground motion in the RADARSAT-2 interferogram (2011/03/22-2011/04/15,
 426 Figure 6d, and fault-normal profile in Figure 7d) would be consistent with slip along a
 427 N-S striking normal fault to the south (green rectangular fault in Figure 7a). After mod-
 428 elling the interferogram covering the co- and post-M4.6 stages (2011/04/15-2011/06/26,
 429 Figure 6f, and fault-normal profile in Figure 7c), Figure 6f shows a different fault seg-

430 ment on a NE-SW trending normal fault to the north (yellow rectangular fault in Fig-
 431 ure 7a). Only one single fault is applied in the modelling above, and the phase caused
 432 by the northern subfault is modelled well due to its dominance during the co- and post-
 433 M4.6 stages. The residual is relatively larger in the south because of the ignorance of
 434 the southern subfault, as the residual phases are shown in Figure S8. Based on modelled
 435 fault geometry in Figure 7a, together with ground motion discontinuities digitised from
 436 the interferograms, we constructed a smooth fault plane with uniformly discretized tri-
 437 angular meshes in Figure 7d. These were generated by FaultResampler (Barnhart & Lohman,
 438 2010) and mesh2d (Engwirda, 2014), with a near-uniform side length of around 125 m.
 439 Then, a fault slip distribution model with associated uncertainties was estimated. We
 440 applied the fault slip inversion method based on a prescribed regularisation derived from
 441 an experimentally validated physics-based crack model (Jiang et al., 2022). To further
 442 investigate the temporal evolution of fault slips with a higher temporal resolution, we
 443 invert the fault slip time series using all available interferograms with clear deformation
 444 signals.

445 Figure 8 presents the temporal evolution of cumulative slip and slip rate during the
 446 2011 Hawthorne seismic swarm, and Figure S9 shows the modelled phase and phase resid-
 447 uals. The findings from the inversion results are listed as follows.

448 (1) There were three areas with different spatio-temporal slipping behaviours: a
 449 narrow (5 km²) slip area on the southern fault with a high rate (with a lower bound: 1.5 cm/day,
 450 or 1.7×10^{-7} m/s) occurring during the pre-M4.6 stage, a wider (15 km²) slip area with
 451 lower average slip (10 cm) on the northern fault that ruptured during the co-M4.6 stage,
 452 and a shallow slip area (depth=1 km) just above the second area during the post-M4.6
 453 stage with a slower average slip rate (with a lower bound: 0.2 cm/day, or 2.3×10^{-8} m/s).

454 (2) Our results show the aseismic slip mainly occurred on the southern subfault dur-
 455 ing the pre-M4.6 stage, while the most significant seismic slip hit the northern subfault
 456 during the co- and post-M4.6 stages. The results are more consistent with a cascade model
 457 of discrete slip patches, rather than a slow-slip model considered as a growing elliptical
 458 crack.

459 (3) During the early pre-M4.6 stage (February 26-March 22), the cumulative geode-
 460 tic moment is 1.7×10^{16} Nm (equivalent to an M_w 4.7 event), 45 times as large as the cu-
 461 mulative seismic moment (0.04×10^{16} Nm). The cumulative geodetic/seismic moment ra-
 462 tio reduces over time, but remains larger than 3 during the co- and post-M4.6 stages.

5 Discussion

5.1 On the Spatial Complexity of Fault Slip Distributions

Fault slip most likely has non-uniform spatial distribution due to spatial heterogeneities of rock strength and stress state on the fault, with well-known dependence on depth and the less understood along-strike variations. Seismic and geodetic inversions can reveal how fault slip is distributed on the discretized fault plane. However, to explore all possible models consistent with observations, the parameter space scales up rapidly to a large number of unknowns, increasing the problem's null-space, which means there are many vectors in the model space that are unconstrained by the data. Therefore, it is reasonable to consider our understanding of the complexity of slip distribution in natural earthquakes. The reasonable approach can allow for fault-slip heterogeneity while keeping the problem null-space as small as possible. Mai and Beroza (2002) compiled published finite-source rupture models and proposed the fractal pattern in slip distributions. It is true for large earthquakes, and multiple fault segments with several rupturing centres are revealed by geodetic and seismological observations, e.g., the 2008 M_w 7.9 Wenchuan earthquake (Shen et al., 2009), and the 2016 M_w 7.8 Kaikoura earthquake (Hamling et al., 2017). However, solving a huge number of parameters has a high computation cost. Computation complexities in their algorithms depend greatly on the number of discretized fault patches. For example, when studying a 40 km-long and 20 km-wide fault with slip-*BERI*, there are 200 patches if the patch size is 2 km and the parameter's dimension is 400. The latter would rapidly increase to 1600 if the patch size is 1 km. This is possibly the reason why the number of imported fault patches has upper bounds in practice, particularly if a Bayesian sampling strategy is employed. Though techniques like parallel computing have been introduced to improve computation efficiency, sampling such high-dimensional problems is still computationally challenging and does not solve the size of the null-space.

In this research effort, we favoured a method that dramatically reduces the number of free parameters to solve; the drawback is that it results in *compact* fault slip distributions. However, our inverted slip distribution patterns are supported by the observations. This is a reasonable approach because many inversion results support fault-slip distributions that are spatially compact, especially for small-magnitude earthquakes (Taymaz et al., 2007; Barnhart et al., 2014; Xu et al., 2016; Champenois et al., 2017; Ainscoe et

495 al., 2017). Many studies have successfully modelled the majority of surface displacement
496 signals using only one single fault with uniform distribution (Biggs et al., 2006; Nissen
497 et al., 2007; Walters et al., 2009). For slow slip events across the global subduction zones,
498 distribution patterns usually follow an elliptical shape with one slipping centre (Wallace
499 et al., 2012; Villegas-Lanza et al., 2016; Fukuda, 2018), and the fractal pattern is not re-
500 quired.

501 Benefiting from the online database of finite fault rupture models, SRCMOD (Mai
502 & Thingbaijam, 2014), we were able to quantitatively evaluate how well a single ellip-
503 tical model fits the available slip distributions across various tectonic settings and mag-
504 nitudes. We retrieved 300 slip distributions on a single fault from SRCMOD and intended
505 to model the slip distributions with the one-ellipse model. Our experiments showed that
506 for 85% of $M_w \leq 7.5$ events, the RMSE of the slip residual is less than 20% of the peak
507 slip (Figure S10). In addition, a simple circular crack is also the widely accepted assumed
508 model in stress drop estimation based on seismic spectra (Madariaga, 1976; Kaneko &
509 Shearer, 2014). Though only small degrees of freedom are allowed in the one-ellipse model,
510 complexity could be added by incorporating multiple ruptures. As we showed in Section
511 2.2, a half-moon pattern was retrieved by two containing or overlapping elliptical crack
512 models. Similarly, it is possible to overlap multiple ruptures to simulate multiple peak
513 slips or more complex patterns.

514 The compact slip distribution in this new elliptical model is also favourable to eval-
515 uate the statistics of small earthquakes. Earthquake source parameters characterisation
516 of small earthquakes is important for understanding the physics of source processes and
517 might be useful for earthquake forecasting (Uchide et al., 2014). A wide-used source model
518 to analyse the source parameters of small earthquakes is a circular crack rupture (Brune,
519 1970; Madariaga, 1976) with stress singularity at the crack tip, and we hope our new el-
520 liptical slip model, which avoids this stress singularity, can be an alternative source model
521 in the future (Shearer et al., 2006). Furthermore, by taking advantage of the improved
522 method for estimating slip rates during temporally overlapping InSAR timeframes, one
523 can image the fault behaviour over a long period in a relatively high temporal resolu-
524 tion. This new method is expected to be applied to investigate the temporal evolution
525 of slow fault slip, e.g., transient slow slip (Khoshmanesh et al., 2015; Kyriakopoulos et
526 al., 2013; Klein et al., 2018), afterslip (Thomas et al., 2014), and slow slip events in sub-
527 duction zones (Bletery & Nocquet, 2020; Rousset et al., 2019; Ozawa et al., 2019).

5.2 Time-dependent Fault Kinematics during Continental Seismic Swarms and Other Slow Earthquakes

During the initial stage of the 2011 Hawthorne seismic swarm, a substantial amount of aseismic slip ruptured on the southern subfault without strong seismicity (e.g., the first two periods in Figure 8b), with peak slip rates of 1.1~5.4 cm/day, average slip rate 0.4~1.9 cm/day and migration velocity 0.05 km/day. Note that these values are the lower bounds of estimation, because the time between two neighbouring epochs (Δs^n) of SAR image acquisition time is regarded as the slow slip duration. The limitation due to the temporal sampling of InSAR could be improved by combining all of the InSAR datasets, or incorporating other high-temporal resolution observations, e.g., GNSS or strainmeter observations. We anticipate that the current InSAR temporal sampling limitation will be reduced over the second half of this decade (2020s). Our approach will be well suited to fully utilise the multiconstellation of InSAR capable satellites (Sentinel-1, CosmoSky-Med, PAZ, TerraSAR-X, ALOS-2, ALOS-4, NISAR, etc.). The phenomena potentially driven by aseismic slip are widely explored, e.g., ETS, Rapid Tremor Reversals (RTRs), SSEs, fault creep, and fluid injection. To better compare this precursory aseismic slip with other identified phenomena in the slow slip family, we compile the slip rates and migration velocities found in the literature list below and in Table S1.

(1) The peak slip rate. SSEs show a wide range of peak slip rates among subduction zones, e.g., 0.27 cm/day for the Cascadia subduction zone (Bletery & Nocquet, 2020), 0.3 cm/day for South Central Alaska Megathrust (Rousset et al., 2019), 0.6~2.8 cm/day for Japan trench (Hirose & Obara, 2010; Ozawa et al., 2019). During the early stage of the 2011 Peloponnese seismic swarm (Greece) (Kyriakopoulos et al., 2013), the fault behaviour was dominated by aseismic slip inferred from the geodetic and seismic moment, and the peak slip rate was 0.26 cm/day. The maximum slip rate in fault creep events is very low, e.g., 0.5 cm/year on the Hayward fault (Schmidt et al., 2005), 0.5 cm/year on the Haiyuan Fault (Jolivet et al., 2012; Song et al., 2019), 0.8 cm/year on the North Anatolia Fault (Hussain et al., 2016) and 3 cm/year on the San Andreas Fault (Johanson & Bürgmann, 2005; Khoshmanesh et al., 2015; Scott et al., 2020). However, in the fluid injection experiment the slow aseismic slip during the early stage was much higher, 4×10^{-3} mm/s (35 cm/day) (Guglielmi et al., 2015), potentially because the measurement in the fluid injection is real-time, and the duration uncertainty is much lower than SSEs observations.

561 (2) The average rate of slip increment. Research on the 2010-2014 seismic swarm
 562 in southern Italy (Cheloni et al., 2017) is consistent with our findings. This research re-
 563 vealed that the average slip rate started to increase two months before the largest shock
 564 (M_w 5.1) and reached the highest value, ~ 0.1 cm/day, a few days before the largest shock.
 565 It then decreased to zero in the following months. This highest average slip rate was at
 566 the same level with ~ 0.4 - 1.9 cm/day in our research. The aseismic slip rate inferred by
 567 RE is much lower, ~ 0.3 - 3 cm/year (Nadeau & McEvilly, 1999; Turner et al., 2013; Mes-
 568 imeri & Karakostas, 2018).

569 (3) Migration velocity. These velocities of ETS and SSEs vary with subduction zones
 570 (Yamashita et al., 2015), but the generally reported migration velocity along the strike
 571 of the plate geometry is ~ 10 km/day (Wech et al., 2009; Wallace et al., 2012), while RTRs
 572 propagate ‘backwards’ 20 to 40 times faster than ETS advances (Houston et al., 2011).
 573 The large-scale features of ETS propagation with RTRs are reproduced and supported
 574 by numerical experiments (Luo & Liu, 2019; Liu et al., 2020). Similarly, migration ve-
 575 locity in TES varies over a wide range, from 0.5 to 14 km/day (Passarelli et al., 2018;
 576 De Barros et al., 2020).

577 **5.3 Spatially variable mechanical response of the Hawthorne swarm faults**

578 As shown in Figure 8b, the southern segment is active during the pre-M4.6 stage,
 579 and the fault behaviour is mostly dominated by aseismic slip, inferred from a very high
 580 geodetic/seismic moment ratio $\in [25, +\infty]$ (Figure 8c), while the general cumulative geode-
 581 tic/seismic moment ratio remains larger than three for the whole seismic swarm. This
 582 significant portion of aseismic slip identified here has been reported associated with a
 583 handful of continental seismic swarms (Lohman & McGuire, 2007; Wicks et al., 2011;
 584 Kyriakopoulos et al., 2013; Gualandi et al., 2017; Cheloni et al., 2017). In 2005, a tec-
 585 tonic swarm of over a thousand earthquakes occurred in the Salton Trough, California
 586 (USA) and Lohman and McGuire (2007) revealed the geodetic moment of the modelled
 587 fault system was about seven times the cumulative seismic moment of the swarm. Wicks
 588 et al. (2011) studied a swarm in southeastern Washington (USA) and also found the geode-
 589 tic/seismic moment ratio was about seven. During the 2011 Peloponnese Peninsula seis-
 590 mic swarm (Greece), Kyriakopoulos et al. (2013) revealed a big discrepancy in moment
 591 release, where the geodetic moment was ~ 5 times the cumulative seismic moment for
 592 the interval July 3-October 1. For the 2013-2014 Northern Apennines seismic swarm (Italy),

593 the moment associated with aseismic deformation/the seismic moment ratio is between
594 $70\% \pm 29\%$ and $200\% \pm 70\%$ (Gualandi et al., 2017). For the 2010-2014 Pollino seis-
595 mic swarm (Italy), Cheloni et al. (2017) found that 70% of the moment was released aseis-
596 mically. Above all, previous studies require aseismic slip to explain the discrepancy be-
597 tween the geodetic moment and seismic moment for seismic swarms, with the estimated
598 ratio of $\sim 5-8$. Furthermore, the compact fault slip identified during the pre-M4.6 stage
599 is favoured by our improved methodology as demonstrated in Section 2. The previous
600 finding of fractal distribution of fault slip is based on M5.9+ earthquakes (Mai & Beroza,
601 2002), while small-to-moderate-magnitude ruptures would have a more compact slip dis-
602 tribution with low complexity as observed in the rupture models SRCMOD (Mai & Thing-
603 baijam, 2014). Therefore, we hope that our improved method can be used to improve
604 the detection of similar small-to-moderate-magnitude aseismic transients in future seis-
605 mic swarms.

606 The large disagreement between the geodetic moment and the seismic moment in-
607 dicates that seismic slip cannot solely explain the observed surface deformation success-
608 fully. Here we test whether the two leading earthquake nucleation hypotheses, the pres-
609 lip model and the cascading model, could be distinguished by using the Coulomb Stress
610 change. (1) To test the preslip model, we calculate the cumulative Coulomb stress changes
611 on the hypocentre of five M4+ foreshocks and the M4.6 event based on the modelled slip.
612 The maximum value of the cumulative Coulomb stress change over the seismic rupture
613 regions is 0.4-6.9 MPa, which is enough to trigger an earthquake (King et al., 1994). Note
614 that there is another possibility that the aseismic slip during the early stage is an inde-
615 pendent slow slip event, and it is not related to the earthquake nucleation and the trig-
616 gering of the M4.6 event is incidental. (2) To test the cascading model, we calculate the
617 cumulative Coulomb stress change on five M4+ events and the M4.6 event caused by the
618 earlier earthquakes and the maximum value of the cumulative Coulomb stress changes
619 over the seismic rupture regions is 0.1-3.0 MPa, which is also higher than 0.01 MPa. It
620 inferred that the M4+ foreshocks and the M4.6 event can also be triggered by the ear-
621 lier earthquakes. However, this analysis can be affected by many factors, e.g., the pre-
622 cision of earthquake hypocentre, and the stress drop calculation method. For example,
623 an $M_w 4.3$ foreshock occurred two hours before the 1992 $M_w 6.1$ Joshua Tree earthquake,
624 and opposite conclusions from two different studies: Dodge et al. (1996) assumed a cir-
625 cular source model with a constant stress drop crack model and the static stress change

626 from the foreshocks was negative by placing the main shock hypocentre inside foreshock
627 rupture; In contrast, Mori (1996) calculated a finite slip model for the foreshock where
628 the mainshock hypocentre was outside of the foreshock rupture, and he estimated a quite
629 high stress drop of the foreshock (32~87 MPa) on the mainshock hypocentre. This con-
630 tradistinction implies the resolution limits of foreshock-location-based triggering anal-
631 ysis. To conclude, as for the largest M4.6 event, we interpret it could have been triggered
632 by earthquake nucleation initiated by aseismic, an independent slow slip event, nearby
633 preceding seismicity, or all of them.

634 The aseismic slip mainly occurred on the southern subfault during the pre-M4.6
635 stage, while the most significant seismic slip hit the northern subfault during the co- and
636 post-M4.6 stages. Here we discuss the possible underlying mechanisms of contrasting be-
637 haviours on the two subfaults. One potential cause of the precursory aseismic slip on the
638 southern segment is various dilatancy properties along the strike. Many authors have
639 studied the shear-induced dilatancy, which could increase the effective normal stress and
640 thus favour fault stability (Segall & Rice, 1995; Segall et al., 2010; Ciardo & Lecampion,
641 2019). For example, to explain abundant microseismicity and aseismic transients in bar-
642 rier zones on the Gofar transform fault, Liu et al. (2020) proposed a numerical model
643 where strong dilatancy strengthening effectively stabilizes along-strike seismic rupture
644 propagation and results in rupture barriers where aseismic transients arise. If this is also
645 true for the 2011 Hawthorne seismic swarm, the shear-induced dilatancy would explain
646 the aseismic transients on the southern fault and the seismic rupture on the northern
647 subfault. What's more, the requirement of enhanced fluid-filled porosity for the dilatancy
648 strengthening might be filled for the 2011 Hawthorne sequence. The 2011 Hawthorne
649 sequence is close to the Aurora-Bodie volcano (Lange & Carmichael, 1996), and geother-
650 mal fluids have been found in this area (Hinz et al., 2010), so it is possible that excess
651 fluids can be persistently supplied and lead to large fluid-filled porosity and high pore
652 pressure. Therefore, the dilatancy strengthening might be one of the underlying mechan-
653 ics that govern the partitioning between aseismic and seismic slip during the 2011 Hawthorne
654 earthquake swarm.

655 In addition, the fault geometrical complexity could favour the lateral variation of
656 slip and aseismic slip. Firstly, Romanet et al. (2018) proposed that two overlapping faults
657 can naturally result in a complex seismic cycle without introducing complex frictional
658 heterogeneities on the fault. They found that for two mildly rate-weakening faults with

659 a small distance between the faults, a complex behaviour with a mixture of slow and rapid
660 slip can be observed. This finding is consistent with the mixture of slow and fast slip close
661 to the connecting region of two subfaults during the 2011 Hawthorne swarm (triangu-
662 lar subfault in Figure 8). Secondly, Cattania and Segall (2021) highlights the effect of
663 long-wavelength fault roughness on a range of fault behaviours, foreshocks, and precur-
664 sory slow slip, during the preparation stage of an energetic event. Their numerical sim-
665 ulation suggested the preparation stage is characterised by feedback between creep and
666 foreshocks: episodic seismic ruptures break neighbouring asperity groups and favour the
667 creep acceleration, which loads other asperities leading to further foreshocks consecu-
668 tively. The coexistence of foreshocks and precursory slow slip, as well as their migration
669 toward the hypocentre of the energetic event in Cattania and Segall (2021), also matched
670 our observation during the pre-4.6 stage (Figure 8). Therefore, we think fault geomet-
671 rical complexity might contribute to the precursory slow slip during the 2011 Hawthorne
672 earthquake swarm.

673 **6 Conclusion**

674 This study developed a new methodology for estimating time-dependent fault slip
675 distributions, by incorporating a physics-based crack model as a regularisation term. We
676 first introduce two propagation patterns of fault ruptures and then propose a method
677 to solve the complex slip distribution with multiple physics-based crack models. Finally,
678 the performance of the proposed methodology is analysed with simulated experiments
679 and geodetic observations during a real seismic swarm case. The advantages of the pro-
680 posed method are as follows.

681 (1) The estimated fault slip solutions describe a compact slip distribution, due to
682 the use of a laboratory-derived crack model. This choice significantly reduces the num-
683 ber of parameters to solve, independently of the subsequent level of fault discretization.
684 Though the slip complexity is less than in the previous methods, the additional complex-
685 ity in the slip pattern can be incorporated by incorporating multiple partially or totally
686 overlapping elliptical cracks.

687 (2) The robustness of our method has been analysed by a) its capability to repro-
688 duce synthetic simulated cases with various slip patterns, and by b) the ability of ellip-
689 tical slip patterns to reproduce published slip distribution from the SRCMOD database.

690 (3) Our proposed method is applied to estimate a detailed time-dependent fault slip dis-

691 tribution model for the 2011 Hawthorne seismic swarm (Nevada, USA). Our results in-
692 dicate that the seismic swarm was caused by activity on a two subfault network with dif-
693 ferent orientations. The results also show that aseismic slip on a southern subfault dom-
694 inates the fault behaviour during a pre-M4.6 stage; after the aseismic pulse (during the
695 most energetic stage), the largest event occurred on a northern subfault. Our results are
696 consistent with an overlapping fault slip migration during the preM4.6 stage along the
697 southern fault, followed by larger triggered coseismic ruptures of fault patches along the
698 northern fault. Our model is consistent with small-scale spatially compact fault slip dis-
699 tribution and allows us to estimate lower bounds for the peak and average value of fault
700 slip rates. These lower-bound estimates are consistent with reported values for slow slip
701 events and other continental swarms.

702 The new inversion method presented here is complementary to the existing method-
703 ologies to estimate fault-slip distributions using geodetic data. We hope that this approach
704 will be particularly useful with current and near-future multiconstellation InSAR satel-
705 lite radar interferometry missions. In this near-future context, this tool could improve
706 the identification of similar precursory (aseismic) slow slip during other long-lasting earth-
707 quake sequences (swarms), and help understand the driving mechanisms of earthquakes.

708 **Acknowledgments**

709 This research was supported by the Natural Environmental Research Council (NERC)
710 through the centre for the Observation and Modelling of Earthquakes, Volcanoes and
711 Tectonics (UK) (GA/13/M/031) and the LiCS large grant (NE/K011006/1). This re-
712 search was also supported by a Chinese Scholarship Council-University of Liverpool joint
713 scholarship awarded to YJ (201706450071). PJG acknowledged the support of the Span-
714 ish Ministerio de Ciencia e Innovación research project, grant agreement number PID2019-
715 104571RA-I00 (COMPACT) and the Beca Leonardo a Investigadores y Creadores Cul-
716 turales 2020 from the Fundación BBVA. RADARSAT-2 images were acquired under SOAR-
717 E project 28209 from the Canadian Space Agency, and ENVISAT images from ESA CAT1
718 project 6745. RADARSAT-2 and ENVISAT interferograms in the paper can be down-
719 loaded from <https://doi.org/10.5281/zenodo.5043161>. The finite-fault source model
720 SRCMOD is retrieved from <http://equake-rc.info/srcmod/>. The geodetic inversion
721 software slipBERI is retrieved from <https://github.com/ruthamey/slipBERI> and WG-
722 BIS package from <https://doi.org/10.5281/zenodo.3727158>. The CRUST 1.0 model
723 is retrieved from <https://igppweb.ucsd.edu/~gabi/crust1.html>. The manuscript was

724 edited by Guido Jones, currently funded by the Cabildo de Tenerife, under the TFinnova
725 Programme supported by MEDI and FDCAN funds. Thanks go to Mehdi Nikkhoo for
726 providing the triangular dislocation functions for the displacement gradient tensor. The
727 authors are also grateful to Tim Wright, Dan Faulkner, and Louisa Brotherson for in-
728 sightful discussions of different aspects of this study, as well as to editor Rachel Aber-
729 crombie, associate editor, Eric Lindsey, and another anonymous reviewer for their help-
730 ful and constructive reviews, which greatly improved this manuscript.

731 **References**

- 732 Ainscoe, E. A., Elliott, J. R., Copley, A., Craig, T. J., Li, T., Parsons, B. E., &
 733 Walker, R. T. (2017). Blind Thrusting, Surface Folding, and the Devel-
 734 opment of Geological Structure in the Mw 6.3 2015 Pishan (China) Earth-
 735 quake. *Journal of Geophysical Research: Solid Earth*, *122*(11), 9359–9382. doi:
 736 10.1002/2017JB014268
- 737 Amey, R. M. J., Hooper, A., & Walters, R. J. (2018). A Bayesian Method for Incor-
 738 porating Self-Similarity into Earthquake Slip Inversions. *Journal of Geophysi-
 739 cal Research: Solid Earth*, *123*(7), 6052–6071. doi: 10.1029/2017JB015316
- 740 Argus, D. F., & Gordon, R. G. (1991). Current Sierra Nevada-North America mo-
 741 tion from very long baseline interferometry: Implications for the kinematics of
 742 the western United States. *Geology*, *19*(11), 1085–1088.
- 743 Aster, R. C., Borchers, B., & Thurber, C. H. (2019). Chapter Three - Rank De-
 744 ficiency and Ill-Conditioning. In R. C. Aster, B. Borchers, & C. H. Thurber
 745 (Eds.), *Parameter Estimation and Inverse Problems* (Third Edition ed., p. 55-
 746 91). Elsevier. doi: 10.1016/B978-0-12-804651-7.00008-0
- 747 Bagnardi, M., & Hooper, A. (2018). Inversion of Surface Deformation Data for
 748 Rapid Estimates of Source Parameters and Uncertainties: A Bayesian Ap-
 749 proach. *Geochemistry, Geophysics, Geosystems*, *19*(7), 2194–2211. doi:
 750 10.1029/2018GC007585
- 751 Barnhart, W. D., Benz, H. M., Hayes, G. P., Rubinstein, J. L., & Bergman,
 752 E. (2014). Seismological and geodetic constraints on the 2011 Mw5.3
 753 Trinidad, Colorado earthquake and induced deformation in the Raton Basin.
 754 *Journal of Geophysical Research: Solid Earth*, *119*(10), 7923–7933. doi:
 755 10.1002/2014JB011227
- 756 Barnhart, W. D., & Lohman, R. B. (2010). Automated fault model discretization
 757 for inversions for coseismic slip distributions. *Journal of Geophysical Research:
 758 Solid Earth*, *115*(B10). doi: 10.1029/2010JB007545
- 759 Barnhart, W. D., Murray, J. R., Briggs, R. W., Gomez, F., Miles, C. P., Svarc, J.,
 760 ... Stressler, B. J. (2016). Coseismic slip and early afterslip of the 2015 Il-
 761 lapel, Chile, earthquake: Implications for frictional heterogeneity and coastal
 762 uplift. *Journal of Geophysical Research: Solid Earth*, *121*(8), 6172–6191. doi:
 763 10.1002/2016JB013124

- 764 Bedford, J., Moreno, M., Baez, J. C., Lange, D., Tilmann, F., Rosenau, M., ... Vi-
765 gny, C. (2013). A high-resolution, time-variable afterslip model for the 2010
766 Maule Mw=8.8, Chile megathrust earthquake. *Earth and Planetary Science*
767 *Letters*, *383*, 26–36. doi: 10.1016/j.epsl.2013.09.020
- 768 Bell, J. W., Amelung, F., & Henry, C. D. (2012). InSAR analysis of the 2008
769 Reno-Mogul earthquake swarm: Evidence for westward migration of Walker
770 Lane style dextral faulting. *Geophysical Research Letters*, *39*(18). doi:
771 10.1029/2012GL052795
- 772 Bennett, R. A., Reilinger, R. E., Rodi, W., Yingping Li, Toksoz, M. N., & Hudnut,
773 K. (1995). Coseismic fault slip associated with the 1992 Mw 6.1 Joshua Tree,
774 California, earthquake: Implications for the Joshua Tree-Landers earthquake
775 sequence. *Journal of Geophysical Research: Solid Earth*, *100*(B4), 6443–6461.
776 doi: 10.1029/94JB02944
- 777 Bhattacharya, P., & Viesca, R. C. (2019). Fluid-induced aseismic fault slip out-
778 paces pore-fluid migration. *Science*, *364*(6439), 464–468. doi: 10.1126/science
779 .aaw7354
- 780 Biggs, J., Bergman, E., Emmerson, B., Funning, G. J., Jackson, J., Parsons, B.,
781 & Wright, T. J. (2006). Fault identification for buried strike-slip earth-
782 quakes using InSAR: The 1994 and 2004 Al Hoceima, Morocco earth-
783 quakes. *Geophysical Journal International*, *166*(3), 1347–1362. doi:
784 10.1111/j.1365-246X.2006.03071.x
- 785 Bletery, Q., & Nocquet, J. M. (2020). Slip bursts during coalescence of slow slip
786 events in Cascadia. *Nature Communications*, *11*(1), 1–6. doi: 10.1038/s41467
787 -020-15494-4
- 788 Bormann, J. M., Hammond, W. C., Kreemer, C., & Blewitt, G. (2016). Accom-
789 modation of missing shear strain in the Central Walker Lane, western North
790 America: Constraints from dense GPS measurements. *Earth and Planetary*
791 *Science Letters*, *440*, 169–177. doi: 10.1016/j.epsl.2016.01.015
- 792 Brune, J. N. (1970). Tectonic stress and the spectra of seismic shear waves from
793 earthquakes. *Journal of Geophysical Research*, *75*(26), 4997–5009. doi: 10
794 .1029/JB075I026P04997
- 795 Bürgmann, R., Ergintav, S., Segall, P., Hearn, E., McClusky, S., Reilinger, R., ...
796 Zschau, J. (2002). Time-Dependent Distributed Afterslip on and Deep be-

- 797 low the İzmit Earthquake Rupture. *Bulletin of the Seismological Society of*
798 *America*, 92, 126–137. doi: 10.1785/0120000833
- 799 Caballero, E., Chounet, A., Duputel, Z., Jara, J., Twardzik, C., & Jolivet, R.
800 (2021). Seismic and Aseismic Fault Slip During the Initiation Phase of the
801 2017 Mw=6.9 Valparaíso Earthquake. *Geophysical Research Letters*, 48(6),
802 e2020GL091916. doi: 10.1029/2020GL091916
- 803 Cappa, F., Scuderi, M. M., Collettini, C., Guglielmi, Y., & Avouac, J. P. (2019).
804 Stabilization of fault slip by fluid injection in the laboratory and in situ. *Sci-*
805 *ence Advances*, 5(3), eaau4065. doi: 10.1126/sciadv.aau4065
- 806 Cattania, C., & Segall, P. (2021). Precursory slow slip and foreshocks on rough
807 faults. *Journal of Geophysical Research: Solid Earth*, e2020JB020430. doi: 10
808 .1029/2020JB020430
- 809 Champenois, J., Baize, S., Vallee, M., Jomard, H., Alvarado, A., Espin, P.,
810 ... Audin, L. (2017). Evidences of Surface Rupture Associated with a
811 Low-Magnitude (Mw 5.0) Shallow Earthquake in the Ecuadorian Andes.
812 *Journal of Geophysical Research: Solid Earth*, 122(10), 8446–8458. doi:
813 10.1002/2017JB013928
- 814 Cheloni, D., D’Agostino, N., Selvaggi, G., Avallone, A., Fornaro, G., Giuliani,
815 R., ... Tizzani, P. (2017). Aseismic transient during the 2010-2014
816 seismic swarm: Evidence for longer recurrence of $M \geq 6.5$ earthquakes in
817 the Pollino gap (Southern Italy)? *Scientific Reports*, 7(1), 1–10. doi:
818 10.1038/s41598-017-00649-z
- 819 Ciardo, F., & Lecampion, B. (2019). Effect of Dilatancy on the Transition from
820 Aseismic to Seismic Slip Due to Fluid Injection in a Fault. *Journal of Geophys-*
821 *ical Research: Solid Earth*, 124(4), 3724–3743. doi: 10.1029/2018JB016636
- 822 De Barros, L., Cappa, F., Deschamps, A., & Dublanchet, P. (2020). Imbricated
823 Aseismic Slip and Fluid Diffusion Drive a Seismic Swarm in the Corinth Gulf,
824 Greece. *Geophysical Research Letters*, 47(9). doi: 10.1029/2020GL087142
- 825 Delorey, A. A., van der Elst, N. J., & Johnson, P. A. (2017). Tidal triggering of
826 earthquakes suggests poroelastic behavior on the San Andreas Fault. *Earth*
827 *and Planetary Science Letters*, 460, 164–170. doi: 10.1016/j.epsl.2016.12.014
- 828 Di Carli, S., François-Holden, C., Peyrat, S., & Madariaga, R. (2010). Dynamic
829 inversion of the 2000 Tottori earthquake based on elliptical subfault ap-

- 830 proximations. *Journal of Geophysical Research*, *115*(B12), B12328. doi:
831 10.1029/2009JB006358
- 832 Dodge, D. A., Beroza, G. C., & Ellsworth, W. L. (1996). Detailed observations of
833 California foreshock sequences: Implications for the earthquake initiation pro-
834 cess. *Journal of Geophysical Research: Solid Earth*, *101*(B10), 22371–22392.
835 doi: 10.1029/96JB02269
- 836 Du, Y., Aydin, A., & Segall, P. (1992). Comparison of various inversion techniques
837 as applied to the determination of a geophysical deformation model for the
838 1983 Borah Peak earthquake. *Bulletin of the Seismological Society of America*,
839 *82*(4), 1840–1866.
- 840 Elliott, J. R., Walters, R. J., England, P. C., Jackson, J. A., Li, Z., & Parsons, B.
841 (2010). Extension on the Tibetan plateau: recent normal faulting measured by
842 InSAR and body wave seismology. *Geophysical Journal International*, *183*(2),
843 503–535. doi: 10.1111/j.1365-246X.2010.04754.x
- 844 Engwirda, D. (2014). *Locally optimal Delaunay-refinement and optimisation-based*
845 *mesh generation* (Doctoral dissertation, University of Sydney). Retrieved from
846 <http://hdl.handle.net/2123/13148>
- 847 Faulds, J., & Henry, C. (2008). Tectonic influences on the spatial and temporal
848 evolution of the Walker Lane: An incipient transform fault along the evolving
849 Pacific - North American plate boundary. *Arizona Geological Society Digest*,
850 *22*, 437–470.
- 851 Floyd, M. A., Walters, R. J., Elliott, J. R., Funning, G. J., Svarc, J. L., Murray,
852 J. R., . . . Wright, T. J. (2016). Spatial variations in fault friction related
853 to lithology from rupture and afterslip of the 2014 South Napa, Califor-
854 nia, earthquake. *Geophysical Research Letters*, *43*(13), 6808–6816. doi:
855 10.1002/2016GL069428
- 856 Fukahata, Y., & Wright, T. J. (2008). A non-linear geodetic data inversion using
857 ABIC for slip distribution on a fault with an unknown dip angle. *Geophysical*
858 *Journal International*, *173*(2), 353–364. doi: 10.1111/j.1365-246X.2007.03713
859 .x
- 860 Fukuda, J. (2018). Variability of the Space-Time Evolution of Slow Slip Events Off
861 the Boso Peninsula, Central Japan, From 1996 to 2014. *Journal of Geophysical*
862 *Research: Solid Earth*, *123*(1), 732–760. doi: 10.1002/2017JB014709

- 863 Fukuda, J., & Johnson, K. M. (2008). A fully Bayesian inversion for spatial distri-
 864 bution of fault slip with objective smoothing. *Bulletin of the Seismological So-*
 865 *ciety of America*, *98*(3), 1128–1146. doi: 10.1785/0120070194
- 866 Fukuda, J., & Johnson, K. M. (2010). Mixed linear-non-linear inversion of crustal
 867 deformation data: Bayesian inference of model, weighting and regularization
 868 parameters. *Geophysical Journal International*, *181*(3), 1441–1458. doi:
 869 10.1111/j.1365-246X.2010.04564.x
- 870 Gavish, M., & Donoho, D. L. (2014). The optimal hard threshold for singular values
 871 is $4/\sqrt{3}$. *IEEE Transactions on Information Theory*, *60*(8), 5040–5053. doi: 10
 872 .1109/TIT.2014.2323359
- 873 Gomberg, J. (2018). Unsettled earthquake nucleation. *Nature Geoscience*, *11*(7),
 874 463–464. doi: 10.1038/s41561-018-0149-x
- 875 Gomberg, J., & Johnson, P. (2005). Dynamic triggering of earthquakes. *Nature*,
 876 *437*(7060), 830. doi: 10.1038/437830a
- 877 González, P. J., Samsonov, S. V., Pepe, S., Tiampo, K. F., Tizzani, P., Casu, F., ...
 878 Sansosti, E. (2013). Magma storage and migration associated with the 2011-
 879 2012 El Hierro eruption: Implications for crustal magmatic systems at oceanic
 880 island volcanoes. *Journal of Geophysical Research: Solid Earth*, *118*(8), 4361–
 881 4377. doi: 10.1002/jgrb.50289
- 882 Grandin, R., Socquet, A., Doin, M.-P., Jacques, E., de Chabalier, J.-B., & King,
 883 G. C. P. (2010). Transient rift opening in response to multiple dike injec-
 884 tions in the Manda Hararo rift (Afar, Ethiopia) imaged by time-dependent
 885 elastic inversion of interferometric synthetic aperture radar data. *Journal of*
 886 *Geophysical Research*, *115*(B9), B09403. doi: 10.1029/2009JB006883
- 887 Gualandi, A., Nichele, C., Serpelloni, E., Chiaraluce, L., Anderlini, L., Latorre, D.,
 888 ... Avouac, J.-P. (2017). Aseismic deformation associated with an earth-
 889 quake swarm in the northern Apennines (Italy). *Geophysical Research Letters*,
 890 *44*(15), 7706–7714. doi: 10.1002/2017GL073687
- 891 Guglielmi, Y., Cappa, F., Avouac, J. P., Henry, P., & Elsworth, D. (2015). Seismic-
 892 ity triggered by fluid injection-induced aseismic slip. *Science*, *348*(6240), 1224–
 893 1226. doi: 10.1126/science.aab0476
- 894 Hamling, I. J., Hreinsdóttir, S., Clark, K., Elliott, J., Liang, C., Fielding, E.,
 895 ... Stirling, M. (2017). Complex multifault rupture during the 2016

- 896 Mw 7.8 Kaikōura earthquake, New Zealand. *Science*, 356(6334). doi:
897 10.1126/science.aam7194
- 898 Hammond, W. C., & Thatcher, W. (2007). Crustal deformation across the Sierra
899 Nevada, northern Walker Lane, Basin and Range transition, western United
900 States measured with GPS, 2000–2004. *Journal of Geophysical Research: Solid
901 Earth*, 112(B5), 5411. doi: 10.1029/2006JB004625
- 902 Harris, R. A., & Segall, P. (1987). Detection of a locked zone at depth on the Park-
903 field, California, segment of the San Andreas Fault. *Journal of Geophysical Re-
904 search*, 92(B8), 7945. doi: 10.1029/JB092iB08p07945
- 905 Hatch, R. L., Abercrombie, R. E., Ruhl, C. J., & Smith, K. D. (2018). Earth-
906 quake Interaction, Fault Structure, and Source Properties of a Small Sequence
907 in 2017 near Truckee, CaliforniaEarthquake Interaction, Fault Structure,
908 and Source Properties of a Small Sequence in 2017 near Truckee. *Bul-
909 letin of the Seismological Society of America*, 108(5A), 2580–2593. doi:
910 10.1785/0120180089
- 911 Hatch, R. L., Abercrombie, R. E., Ruhl, C. J., & Smith, K. D. (2020). Evidence of
912 Aseismic and Fluid-Driven Processes in a Small Complex Seismic Swarm Near
913 Virginia City, Nevada. *Geophysical Research Letters*, 47(4), e2019GL085477.
914 doi: 10.1029/2019GL085477
- 915 Hatch-Ibarra, R. L., Abercrombie, R. E., Ruhl, C. J., Smith, K. D., Hammond,
916 W. C., & Pierce, I. K. (2022). The 2016 Nine Mile Ranch Earthquakes:
917 Hazard and Tectonic Implications of Orthogonal Conjugate Faulting in
918 the Walker Lane. *Bulletin of the Seismological Society of America*. doi:
919 10.1785/0120210149
- 920 Hicks, S. P., Okuwaki, R., Steinberg, A., Rychert, C. A., Harmon, N., Abercrombie,
921 R. E., . . . Sudhaus, H. (2020). Back-propagating supershear rupture in the
922 2016 Mw 7.1 Romanche transform fault earthquake. *Nature Geoscience*, 13(9),
923 647–653. doi: 10.1038/s41561-020-0619-9
- 924 Hinz, N., Faulds, J., Moeck, I., Bell, J. W., & Oldow, J. S. (2010). Structural con-
925 trols of three blind geothermal resources at the hawthorne ammunition depot,
926 West-Central Nevada. *Transactions - Geothermal Resources Council*, 34,
927 720–725.
- 928 Hirose, H., & Obara, K. (2010). Recurrence behavior of short-term slow slip

- 929 and correlated nonvolcanic tremor episodes in western Shikoku, southwest
930 Japan. *Journal of Geophysical Research: Solid Earth*, 115(B6), 0–21. doi:
931 10.1029/2008JB006050
- 932 Houston, H., Delbridge, B. G., Wech, A. G., & Creager, K. C. (2011). Rapid tremor
933 reversals in Cascadia generated by a weakened plate interface. *Nature Geo-*
934 *science*, 4(6), 404–409. doi: 10.1038/ngeo1157
- 935 Hussain, E., Hooper, A., Wright, T. J., Walters, R. J., & Bekaert, D. P. (2016).
936 Interseismic strain accumulation across the central North Anatolian Fault from
937 iteratively unwrapped InSAR measurements. *Journal of Geophysical Research:*
938 *Solid Earth*, 121(12), 9000–9019. doi: 10.1002/2016JB013108
- 939 Ichinose, G. A., Anderson, J. G., Smith, K. D., & Zeng, Y. (2003). Source Param-
940 eters of Eastern California and Western Nevada Earthquakes from Regional
941 Moment Tensor Inversion. *Bulletin of the Seismological Society of America*,
942 93(1), 61–84. doi: 10.1785/0120020063
- 943 Ingleby, T., Wright, T. J., Hooper, A., Craig, T. J., & Elliott, J. R. (2020). Con-
944 straints on the Geometry and Frictional Properties of the Main Himalayan
945 Thrust Using Coseismic, Postseismic, and Interseismic Deformation in Nepal.
946 *Journal of Geophysical Research: Solid Earth*, 125(2), e2019JB019201. doi:
947 10.1029/2019JB019201
- 948 Jiang, Y., & González, P. J. (2020). Bayesian Inversion of Wrapped Satellite
949 Interferometric Phase to Estimate Fault and Volcano Surface Ground Defor-
950 mation Models. *Journal of Geophysical Research: Solid Earth*, 125(5). doi:
951 10.1029/2019JB018313
- 952 Jiang, Y., & González, P. J. (2021). High-resolution spatio-temporal fault slip using
953 InSAR observations: insights on seismic and aseismic slip during a shallow
954 crust earthquake swarm. In *EGU General Assembly Conference Abstracts*. doi:
955 10.5194/egusphere-egu21-6280
- 956 Jiang, Y., González, P. J., & Bürgmann, R. (2022). Subduction earthquakes con-
957 trolled by incoming plate geometry: The 2020 $M > 7.5$ Shumagin, Alaska,
958 earthquake doublet. *Earth and Planetary Science Letters*, 584, 117447. doi:
959 10.1016/J.EPSL.2022.117447
- 960 Johanson, I. A., & Bürgmann, R. (2005). Creep and quakes on the northern tran-
961 sition zone of the San Andreas fault from GPS and InSAR data. *Geophysical*

- 962 *Research Letters*, 32(14), 1–5. doi: 10.1029/2005GL023150
- 963 Johnson, K. M., Fukuda, J., & Segall, P. (2012). Challenging the rate-state as-
 964 perity model: Afterslip following the 2011 M9 Tohoku-oki, Japan, earth-
 965 quake. *Geophysical Research Letters*, 39(20), 2012GL052901. doi:
 966 10.1029/2012GL052901
- 967 Jolivet, R., Lasserre, C., Doin, M. P., Guillaso, S., Peltzer, G., Dailu, R., . . . Xu, X.
 968 (2012). Shallow creep on the Haiyuan Fault (Gansu, China) revealed by SAR
 969 Interferometry. *Journal of Geophysical Research: Solid Earth*, 117(B6), 6401.
 970 doi: 10.1029/2011JB008732
- 971 Kampes, B., Hanssen, R., & Perski, Z. (2003). Radar interferometry with public do-
 972 main tools. *Proc. of FRINGE 2003 Workshop*.
- 973 Kaneko, Y., & Shearer, P. M. (2014). Seismic source spectra and estimated stress
 974 drop derived from cohesive-zone models of circular subshear rupture. *Geophys-
 975 ical Journal International*, 197(2), 1002–1015. doi: 10.1093/gji/ggu030
- 976 Ke, C.-Y., McLaskey, G. C., & Kammer, D. S. (2020). The Earthquake Arrest Zone.
 977 *Geophysical Journal International*. doi: 10.1093/gji/ggaa386
- 978 Khoshmanesh, M., Shirzaei, M., & Nadeau, R. M. (2015). Time-dependent model
 979 of aseismic slip on the central San Andreas Fault from InSAR time series and
 980 repeating earthquakes. *Journal of Geophysical Research: Solid Earth*, 120(9),
 981 6658–6679. doi: 10.1002/2015JB012039
- 982 King, G. C. P., Stein, R. S., & Lin, J. (1994). Static stress changes and the trig-
 983 gering of earthquakes. *Bulletin of the Seismological Society of America*, 84(3),
 984 935–953.
- 985 Klein, E., Duputel, Z., Zigone, D., Vigny, C., Boy, J.-P., Doubre, C., & Meneses,
 986 G. (2018). Deep transient slow slip detected by survey gps in the region of
 987 atacama, chile. *Geophysical Research Letters*, 45(22), 12,263–12,273. doi:
 988 10.1029/2018GL080613
- 989 Kreemer, C., Blewitt, G., & Hammond, W. C. (2009). Geodetic constraints on
 990 contemporary deformation in the northern Walker Lane: 2. Velocity and
 991 strain rate tensor analysis. In *Late Cenozoic Structure and Evolution of the
 992 Great Basin-Sierra Nevada Transition*. Geological Society of America. doi:
 993 10.1130/2009.2447(02)
- 994 Kreemer, C., Blewitt, G., & Klein, E. C. (2014). A geodetic plate motion and Global

- 995 Strain Rate Model. *Geochemistry, Geophysics, Geosystems*, 15(10), 3849–3889.
 996 doi: 10.1002/2014GC005407
- 997 Kyriakopoulos, C., Chini, M., Bignami, C., Stramondo, S., Ganas, A., Kolligri, M.,
 998 & Moshou, A. (2013). Monthly migration of a tectonic seismic swarm detected
 999 by DInSAR: Southwest Peloponnese, Greece. *Geophysical Journal Interna-*
 1000 *tional*, 194(3), 1302–1309. doi: 10.1093/gji/ggt196
- 1001 Lambert, V., Lapusta, N., & Perry, S. (2021). Propagation of large earthquakes as
 1002 self-healing pulses or mild cracks. *Nature*, 591(7849), 252–258. doi: 10.1038/
 1003 s41586-021-03248-1
- 1004 Lange, R. A., & Carmichael, I. S. E. (1996). The Aurora volcanic field, California-
 1005 Nevada: oxygen fugacity constraints on the development of andesitic
 1006 magma. *Contributions to Mineralogy and Petrology*, 125(2), 167–185. doi:
 1007 10.1007/s004100050214
- 1008 Liu, Y., McGuire, J. J., & Behn, M. D. (2020). Aseismic transient slip on the Go-
 1009 far transform fault, East Pacific Rise. *Proceedings of the National Academy of*
 1010 *Sciences of the United States of America*, 117(19), 10188–10194. doi: 10.1073/
 1011 pnas.1913625117
- 1012 Lohman, R. B., & McGuire, J. J. (2007). Earthquake swarms driven by aseismic
 1013 creep in the Salton Trough, California. *Journal of Geophysical Research: Solid*
 1014 *Earth*, 112(4). doi: 10.1029/2006JB004596
- 1015 Luo, Y., & Liu, Z. (2019). Rate-and-State Model Casts New Insight into Episodic
 1016 Tremor and Slow-slip Variability in Cascadia. *Geophysical Research Letters*,
 1017 46(12), 6352–6362. doi: 10.1029/2019GL082694
- 1018 Madariaga, R. (1976). Dynamics of an expanding circular fault. *Bulletin of the Seis-*
 1019 *mological Society of America*, 66(3), 639–666.
- 1020 Mai, P. M., & Beroza, G. C. (2002). A spatial random field model to characterize
 1021 complexity in earthquake slip. *Journal of Geophysical Research: Solid Earth*,
 1022 107(B11), ESE 10–1–ESE 10–21. doi: 10.1029/2001jb000588
- 1023 Mai, P. M., & Thingbaijam, K. K. (2014). SRCMOD: An online database of finite-
 1024 fault rupture models. *Seismological Research Letters*, 85(6), 1348–1357. doi:
 1025 10.1785/0220140077
- 1026 Marone, C., & Richardson, E. (2006). Do earthquakes rupture piece by piece or all
 1027 together? *Science*, 313(5794), 1748–1749. doi: 10.1126/science.1131296

- 1028 Matthews, M. V., & Segall, P. (1993). Estimation of depth-dependent fault slip
 1029 from measured surface deformation with application to the 1906 San Francisco
 1030 earthquake. *Journal of Geophysical Research*, *98*(B7), 12153–12163. doi:
 1031 10.1029/93jb00440
- 1032 Mesimeri, M., & Karakostas, V. (2018). Repeating earthquakes in western Corinth
 1033 Gulf (Greece): Implications for aseismic slip near locked faults. *Geophysical*
 1034 *Journal International*, *215*(1), 659–676. doi: 10.1093/gji/ggy301
- 1035 Michel, S., Gualandi, A., & Avouac, J. P. (2019). Similar scaling laws for earth-
 1036 quakes and Cascadia slow-slip events. *Nature*, *574*(7779), 522–526. doi: 10
 1037 .1038/s41586-019-1673-6
- 1038 Minson, S. E., Simons, M., & Beck, J. L. (2013). Bayesian inversion for finite fault
 1039 earthquake source models I—theory and algorithm. *Geophysical Journal Inter-*
 1040 *national*, *194*(3), 1701–1726. doi: 10.1093/gji/ggt180
- 1041 Mori, J. (1996). Rupture directivity and slip distribution of the M 4.3 foreshock to
 1042 the 1992 Joshua Tree earthquake, Southern California. *Bulletin of the Seismo-*
 1043 *logical Society of America*, *86*(3), 805–810. doi: 10.1785/BSSA0860030805
- 1044 Nadeau, R. M., & McEvilly, T. V. (1999). Fault slip rates at depth from recurrence
 1045 intervals of repeating microearthquakes. *Science*, *285*(5428), 718–721. doi: 10
 1046 .1126/science.285.5428.718
- 1047 Nissen, E., Ghorashi, M., Jackson, J., Parsons, B., & Talebian, M. (2007). The
 1048 2005 Qeshm Island earthquake (Iran) - A link between buried reverse faulting
 1049 and surface folding in the Zagros Simply Folded Belt? *Geophysical Journal*
 1050 *International*, *171*(1), 326–338. doi: 10.1111/j.1365-246X.2007.03514.x
- 1051 Ozawa, S., Yarai, H., & Kobayashi, T. (2019). Recovery of the recurrence interval of
 1052 Boso slow slip events in Japan. *Earth, Planets and Space*, *71*(1), 1–8. doi: 10
 1053 .1186/s40623-019-1058-y
- 1054 Parotidis, M., Rothert, E., & Shapiro, S. A. (2003). Pore-pressure diffu-
 1055 sion: A possible triggering mechanism for the earthquake swarms 2000 in
 1056 Vogtland/NW-Bohemia, central Europe. *Geophysical Research Letters*, *30*(20),
 1057 2003GL018110. doi: 10.1029/2003GL018110
- 1058 Passarelli, L., Rivalta, E., Jónsson, S., Hensch, M., Metzger, S., Jakobsdóttir, S. S.,
 1059 ... Dahm, T. (2018). Scaling and spatial complementarity of tectonic
 1060 earthquake swarms. *Earth and Planetary Science Letters*, *482*, 62–70. doi:

- 1061 10.1016/j.epsl.2017.10.052
- 1062 Pritchard, M. E., & Simons, M. (2006). An aseismic slip pulse in northern Chile
1063 and along-strike variations in seismogenic behavior. *Journal of Geophysical Re-*
1064 *search: Solid Earth*, *111*(8). doi: 10.1029/2006JB004258
- 1065 Radiguet, M., Cotton, F., Vergnolle, M., Campillo, M., Valette, B., Kostoglodov, V.,
1066 & Cotte, N. (2011). Spatial and temporal evolution of a long term slow slip
1067 event: the 2006 Guerrero Slow Slip Event. *Geophysical Journal International*,
1068 *184*(2), 816–828. doi: 10.1111/j.1365-246X.2010.04866.x
- 1069 Radiguet, M., Perfettini, H., Cotte, N., Gualandi, A., Valette, B., Kostoglodov, V.,
1070 ... Campillo, M. (2016). Triggering of the 2014 Mw7.3 Papanoa earthquake
1071 by a slow slip event in Guerrero, Mexico. *Nature Geoscience* *2016 9:11*, *9*(11),
1072 829–833. doi: 10.1038/ngeo2817
- 1073 Ragon, T., Sladen, A., & Simons, M. (2018). Accounting for uncertain fault geome-
1074 try in earthquake source inversions – I: theory and simplified application. *Geo-*
1075 *physical Journal International*, *214*(2), 1174–1190. doi: 10.1093/gji/ggy187
- 1076 Romanet, P., Bhat, H. S., Jolivet, R., & Madariaga, R. (2018). Fast and Slow Slip
1077 Events Emerge Due to Fault Geometrical Complexity. *Geophysical Research*
1078 *Letters*, *45*(10), 4809–4819. doi: 10.1029/2018GL077579
- 1079 Rousset, B., Fu, Y., Bartlow, N., & Bürgmann, R. (2019). Weeks-Long and Years-
1080 Long Slow Slip and Tectonic Tremor Episodes on the South Central Alaska
1081 Megathrust. *Journal of Geophysical Research: Solid Earth*, *124*(12), 13392–
1082 13403. doi: 10.1029/2019JB018724
- 1083 Ruhl, C. J., Abercrombie, R. E., Smith, K. D., & Zaliapin, I. (2016). Complex
1084 spatiotemporal evolution of the 2008 Mw 4.9 Mogul earthquake swarm (Reno,
1085 Nevada): Interplay of fluid and faulting. *Journal of Geophysical Research:*
1086 *Solid Earth*, *121*(11), 8196–8216. doi: 10.1002/2016JB013399
- 1087 Ruhl, C. J., Morton, E. A., Bormann, J. M., Hatch-Ibarra, R., Ichinose, G., &
1088 Smith, K. D. (2021). Complex Fault Geometry of the 2020 Mww 6.5 Monte
1089 Cristo Range, Nevada, Earthquake Sequence. *Seismological Research Letters*,
1090 *92*, 1876–1890. doi: 10.1785/0220200345
- 1091 Salman, R., Hill, E. M., Feng, L., Lindsey, E. O., Mele Veedu, D., Barbot, S., ...
1092 Natawidjaja, D. H. (2017). Piecemeal Rupture of the Mentawai Patch, Suma-
1093 tra: The 2008 Mw 7.2 North Pagai Earthquake Sequence. *Journal of Geophys-*

- 1094 *ical Research: Solid Earth*, 122(11), 9404–9419. doi: 10.1002/2017JB014341
- 1095 Samsonov, S., & D’Oreye, N. (2012). Multidimensional time-series analysis of
1096 ground deformation from multiple InSAR data sets applied to Virunga Vol-
1097 canic Province. *Geophysical Journal International*, 191(3), 1095–1108. doi:
1098 10.1111/j.1365-246X.2012.05669.x
- 1099 Schmidt, D. A., Bürgmann, R., Nadeau, R. M., & D’Alessio, M. (2005). Distribution
1100 of aseismic slip rate on the Hayward fault inferred from seismic and geode-
1101 tic data. *Journal of Geophysical Research: Solid Earth*, 110(B8), 1–15. doi:
1102 10.1029/2004JB003397
- 1103 Scott, C., Bunds, M., Shirzaei, M., & Toke, N. (2020). Creep Along the Central San
1104 Andreas Fault From Surface Fractures, Topographic Differencing, and InSAR.
1105 *Journal of Geophysical Research: Solid Earth*, 125(10), e2020JB019762. doi:
1106 10.1029/2020JB019762
- 1107 Segall, P., & Rice, J. R. (1995). Dilatancy, compaction, and slip instability of a
1108 fluid-infiltrated fault. *Journal of Geophysical Research: Solid Earth*, 100(B11),
1109 22155–22171. doi: 10.1029/95JB02403
- 1110 Segall, P., Rubin, A. M., Bradley, A. M., & Rice, J. R. (2010). Dilatant strength-
1111 ening as a mechanism for slow slip events. *Journal of Geophysical Research*,
1112 115(B12), B12305. doi: 10.1029/2010JB007449
- 1113 Shearer, P. M., Prieto, G. A., & Hauksson, E. (2006). Comprehensive analysis of
1114 earthquake source spectra in southern California. *Journal of Geophysical Re-
1115 search: Solid Earth*, 111(B6), 6303. doi: 10.1029/2005JB003979
- 1116 Shen, Z. K., Sun, J., Zhang, P., Wan, Y., Wang, M., Bürgmann, R., . . . Wang,
1117 Q. (2009). Slip maxima at fault junctions and rupturing of barriers during
1118 the 2008 Wenchuan earthquake. *Nature Geoscience*, 2(10), 718–724. doi:
1119 10.1038/ngeo636
- 1120 Smith, K., Johnson, C., Davies, J., Agbaje, T., Knezevic Antonijevic, S., & Kent, G.
1121 (2011). The 2011 Hawthorne, Nevada, Earthquake Sequence: Shallow Normal
1122 Faulting. In *AGU Fall Meeting* (pp. S53B–2284).
- 1123 Song, X., Jiang, Y., Shan, X., Gong, W., & Qu, C. (2019). A Fine Velocity and
1124 Strain Rate Field of Present-Day Crustal Motion of the Northeastern Tibetan
1125 Plateau Inverted Jointly by InSAR and GPS. *Remote Sensing 2019, Vol. 11*,
1126 *Page 435*, 11(4), 435. doi: 10.3390/RS11040435

- 1127 Stein, S., & Gordon, R. G. (1984). Statistical tests of additional plate boundaries
1128 from plate motion inversions. *Earth and Planetary Science Letters*, *69*(2), 401–
1129 412. doi: 10.1016/0012-821X(84)90198-5
- 1130 Sun, J., Johnson, K. M., Cao, Z., Shen, Z., Bürgmann, R., & Xu, X. (2011). Me-
1131chanical constraints on inversion of coseismic geodetic data for fault slip and
1132 geometry: Example from InSAR observation of the 6 October 2008 Mw 6.3
1133 Dangxiong-Yangyi (Tibet) earthquake. *Journal of Geophysical Research*,
1134 *116*(B1), B01406. doi: 10.1029/2010JB007849
- 1135 Takenaka, H., & Fujii, Y. (2008). A compact representation of spatio-temporal slip
1136 distribution on a rupturing fault. *Journal of Seismology*, *12*, 281-293. doi: 10
1137 .1007/s10950-007-9087-6
- 1138 Taymaz, T., Wright, T. J., Yolsal, S., Tan, O., Fielding, E., & Seyitoğlu, G. (2007).
1139 Source characteristics of the 6 June 2000 Orta-Çankiri (central Turkey) earth-
1140 quake: A synthesis of seismological, geological and geodetic (InSAR) obser-
1141 vations, and internal deformation of the Anatolian plate. *Geological Society*
1142 *Special Publication*, *291*(1), 259–290. doi: 10.1144/SP291.12
- 1143 Thomas, M. Y., Avouac, J.-P., Champenois, J., Lee, J.-C., Kuo, L.-C., Thomas,
1144 M. Y., . . . Kuo, L.-C. (2014). Spatiotemporal evolution of seismic and aseis-
1145 mic slip on the Longitudinal Valley Fault, Taiwan. *Journal of Geophysical*
1146 *Research: Solid Earth*, *119*(6), 5114–5139. doi: 10.1002/2013JB010603
- 1147 Tridon, M., Cayol, V., Froger, J., Augier, A., & Bachèlery, P. (2016). Inversion of co-
1148 eval shear and normal stress of Piton de la Fournaise flank displacement. *Jour-
1149 nal of Geophysical Research: Solid Earth*, *121*(11), 7846–7866. doi: 10.1002/
1150 2016JB013330
- 1151 Tsang, L. L. H., Hill, E. M., Barbot, S., Qiu, Q., Feng, L., Hermawan, I., . . . Nataw-
1152 idjaja, D. H. (2016). Afterslip following the 2007 Mw 8.4 Bengkulu earthquake
1153 in Sumatra loaded the 2010 Mw 7.8 Mentawai tsunami earthquake rupture
1154 zone. *Journal of Geophysical Research: Solid Earth*, *121*(12), 9034–9049. doi:
1155 10.1002/2016JB013432
- 1156 Turner, R. C., Nadeau, R. M., & Bürgmann, R. (2013). Aseismic slip and fault in-
1157 teraction from repeating earthquakes in the Loma Prieta aftershock zone. *Geo-
1158 physical Research Letters*, *40*(6), 1079–1083. doi: 10.1002/grl.50212
- 1159 Uchide, T., Shearer, P. M., & Imanishi, K. (2014). Stress drop variations among

- 1160 small earthquakes before the 2011 Tohoku-oki, Japan, earthquake and impli-
 1161 cations for the main shock. *Journal of Geophysical Research: Solid Earth*,
 1162 *119*(9), 7164–7174. doi: 10.1002/2014JB010943
- 1163 Villegas-Lanza, J. C., Nocquet, J. M., Rolandone, F., Vallee, M., Tavera, H., Bon-
 1164 doux, F., . . . Chlieh, M. (2016). A mixed seismic-aseismic stress release
 1165 episode in the Andean subduction zone. *Nature Geoscience*, *9*(2), 150–154.
 1166 doi: 10.1038/ngeo2620
- 1167 Wallace, L. M. (2020). Slow Slip Events in New Zealand. *Annual Review of Earth*
 1168 *and Planetary Sciences*, *48*(1), 175–203. doi: 10.1146/annurev-earth-071719
 1169 -055104
- 1170 Wallace, L. M., Beavan, J., Bannister, S., & Williams, C. (2012). Simultaneous long-
 1171 term and short-term slow slip events at the Hikurangi subduction margin, New
 1172 Zealand: Implications for processes that control slow slip event occurrence,
 1173 duration, and migration. *Journal of Geophysical Research B: Solid Earth*,
 1174 *117*(11). doi: 10.1029/2012JB009489
- 1175 Walters, R. J., Elliott, J. R., D’Agostino, N., England, P. C., Hunstad, I., Jackson,
 1176 J. A., . . . Roberts Edinburgh, G. (2009). The 2009 L’Aquila earthquake
 1177 (central Italy): A source mechanism and implications for seismic hazard. *Geo-*
 1178 *physical Research Letters*, *36*(17). doi: 10.1029/2009GL039337
- 1179 Wech, A. G., Creager, K. C., & Melbourne, T. I. (2009). Seismic and geodetic con-
 1180 straints on Cascadia slow slip. *Journal of Geophysical Research: Solid Earth*,
 1181 *114*(10). doi: 10.1029/2008JB006090
- 1182 Werner, C. (2000). GAMMA SAR and interferometric processing software. *Proceed-*
 1183 *ings of ERS-Envisat Symposium ; 16-20 October, Gothenburg, Sweden, 2000*.
- 1184 Wesnousky, S. (2005). Active faulting in the Walker Lane. *Tectonics*, *24*(3). doi: 10
 1185 .1029/2004TC001645
- 1186 Wicks, C., Thelen, W., Weaver, C., Gomberg, J., Rohay, A., & Bodin, P. (2011).
 1187 InSAR observations of aseismic slip associated with an earthquake swarm in
 1188 the Columbia River flood basalts. *Journal of Geophysical Research*, *116*(B12),
 1189 B12304. doi: 10.1029/2011JB008433
- 1190 Xu, W., Bürgmann, R., & Li, Z. (2016). An improved geodetic source model for the
 1191 1999 Mw 6.3 Chamoli earthquake, India. *Geophysical Journal International*,
 1192 *205*(1), 236–242. doi: 10.1093/gji/ggw016

- 1193 Yamashita, Y., Yakiwara, H., Asano, Y., Shimizu, H., Uchida, K., Hirano, S., ...
1194 Obara, K. (2015). Migrating tremor off southern Kyushu as evidence for
1195 slow slip of a shallow subduction interface. *Science*, *348*(6235), 676–679. doi:
1196 10.1126/science.aaa4242
- 1197 Zha, X., Jia, Z., Dai, Z., & Lu, Z. (2019). The cause of the 2011 Hawthorne
1198 (Nevada) earthquake swarm constrained by seismic and InSAR methods.
1199 *Journal of Geodesy*, *93*(6), 899–909. doi: 10.1007/s00190-018-1212-5

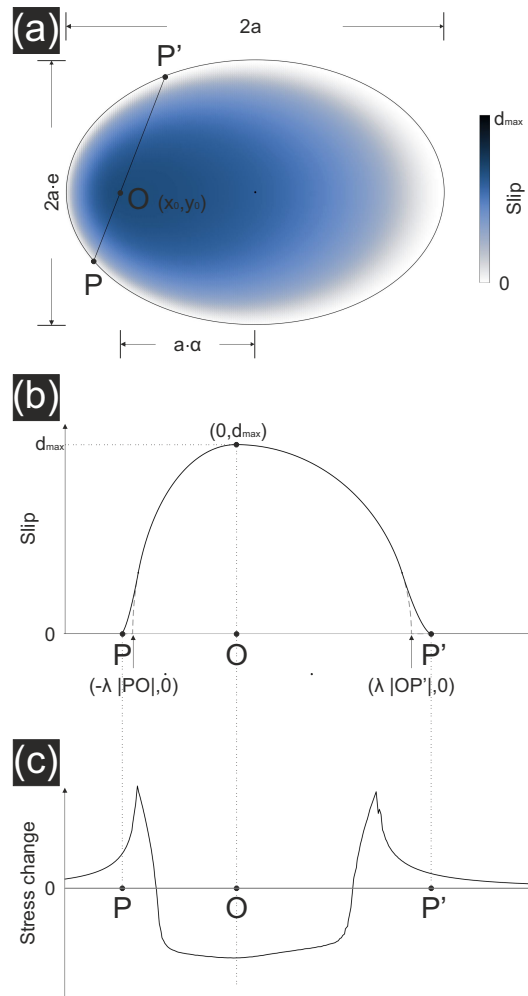


Figure 1. Parameters of the proposed slip model. Image (a) shows the 2d slip distribution, with an elliptical shape. The slip and stress changes along profile POP' are presented in images (b)-(c).

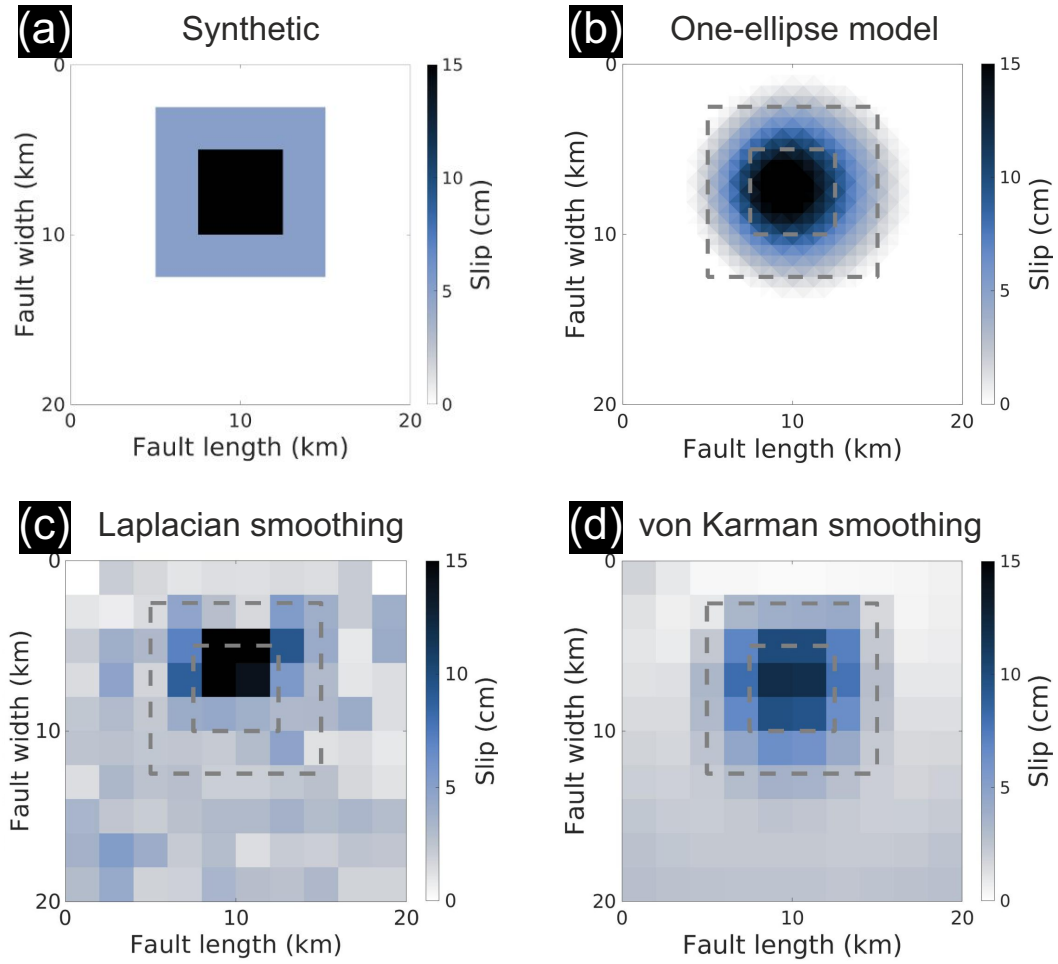


Figure 2. Synthetic and modelled fault slip distribution for a synthetic case. Image (a) shows the synthetic non-uniform slip distribution on a simulated fault plane. The black area is a $5 \text{ km} \times 5 \text{ km}$ region with 15 cm down-dip slip. The blue area is a $10 \text{ km} \times 10 \text{ km}$ region with 5 cm down-dip slip. No slip occurs in the white area. Images (b)-(d) are the inverted fault slip distribution based on the optimal model with maximum likelihood estimated by the one-ellipse model (GICMo), the Laplacian smoothing and the von Karman smoothing (slipBERI). The dashed line in image (b)-(d) indicate the boundary of various slipping area in image (a).

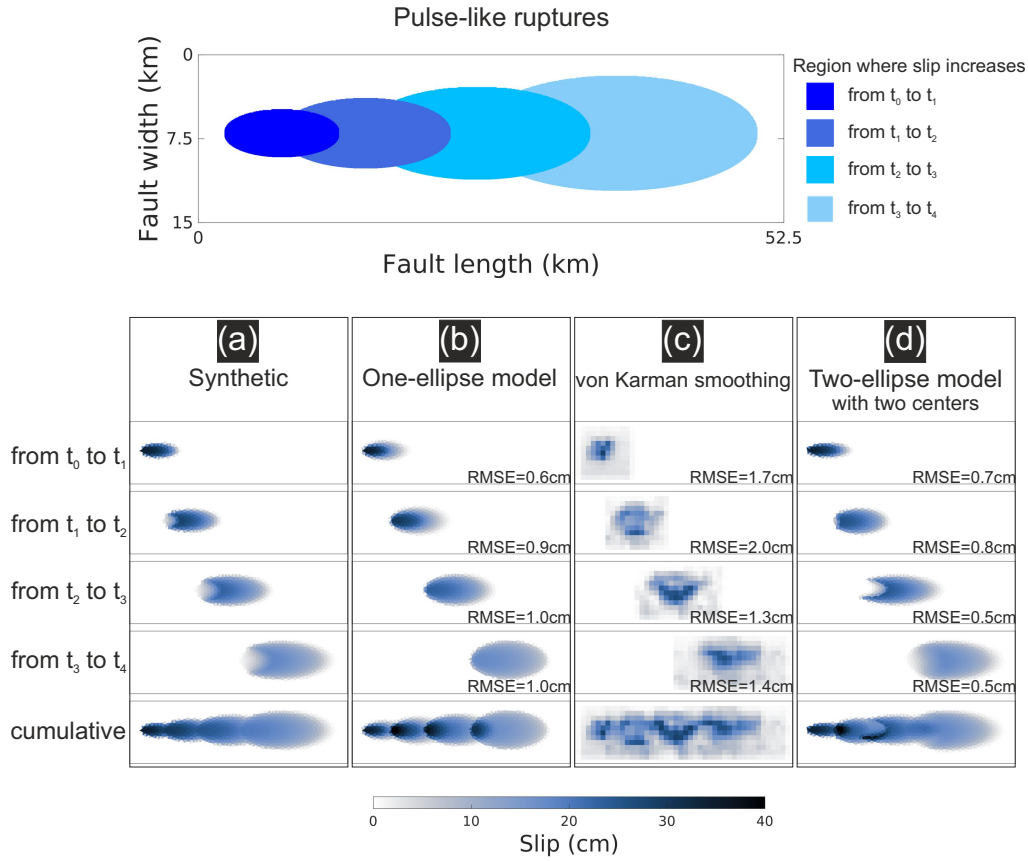


Figure 3. Synthetic and modelled fault slip distributions for synthetic case 2 (pulse-like ruptures). The top image is the conceptual diagram representing the growing cracks with the overlapping relationship. Images in column (a) show the synthetic slip increments. Images in columns (b)-(d) show the modelled slip distribution with various inversion methods: the one-ellipse model (b), the von Karman smoothing (c), and the two-ellipse model with different centres (d), and the RMSE of the slip residuals are shown at the bottom right.

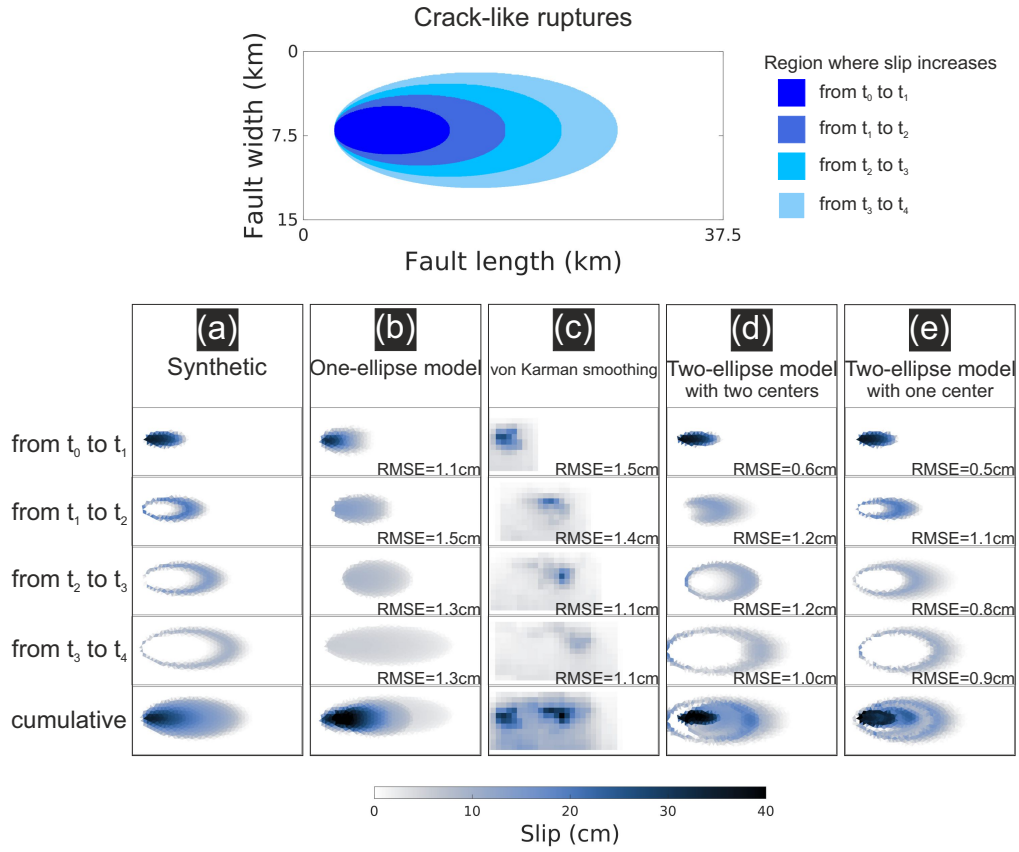


Figure 4. Synthetic and modelled fault slip distribution for synthetic case 2 (crack-like ruptures). The top image is the conceptual diagram presenting the growing cracks with the containing relationship. Images in column (a) show the synthetic slip increments. Images in columns (b)-(e) show the modelled slip distribution with various inversion methods: the one-ellipse model (b), the von Karman smoothing (c), the two-ellipse model with different centres (d) and with the same centre (e), and the RMSE of the slip residuals are shown at the bottom right.

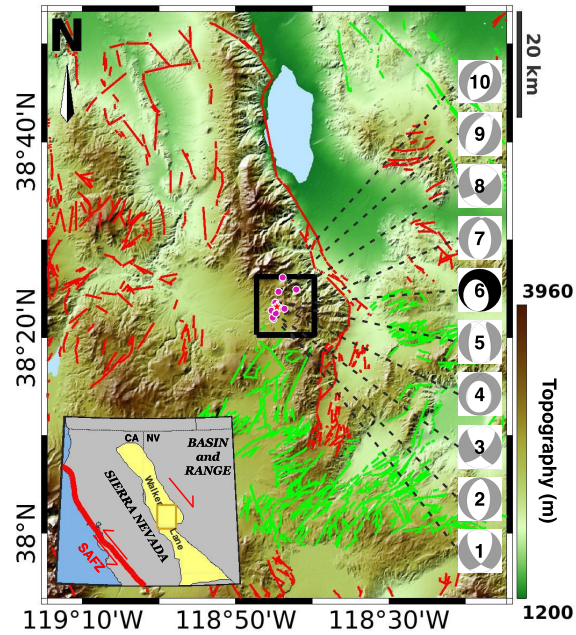


Figure 5. Tectonic settings for the 2011 Hawthorne seismic swarm. Image (a) shows the structural geologic environment of Walker Lane, located between the Sierra Nevada microplate and Basin and Range Province. It accommodates relative motion between the Pacific and North America. The brown rectangular box is the boundary of image (b), the central segment of Walker Lane. Image (b) shows the detailed tectonic settings for the 2011 Hawthorne seismic swarm, with topography as the base map. Normal and strike-slip faults are plotted as red and green lines. The beach balls on the right show the focal mechanism solutions provided by the Nevada Seismological Laboratory (Ichinose et al., 2003). Beach ball No.6 in black is the event with the largest magnitude, M4.6. Abbreviation: SAFZ, San Andreas Fault Zone.

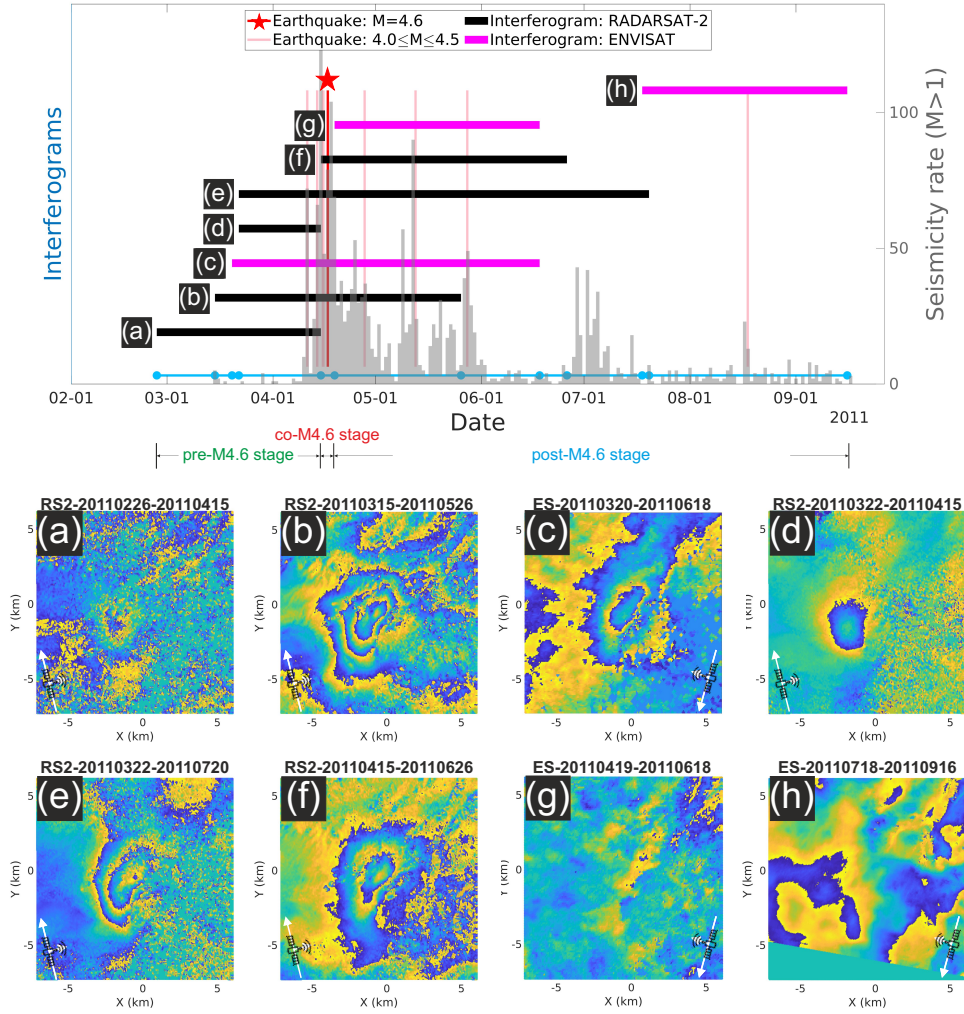


Figure 6. Surface displacement observations for the 2011 Hawthorne seismic swarm. In this research, the 2011 Hawthorne seismic swarm is divided into 3 stages with respect to the largest event, M4.6 on April 17 2011 (red star in the top image): pre-, co- and post-M4.6 event. The top image shows the time coverage of the interferograms (horizontal lines) over $M \geq 4$ events (vertical lines). Out of 8 interferograms (a)-(h), 5 are from RADARSAT-2 (black lines) and 3 from ENVISAT (magenta lines). For the blue line at the bottom, dots infer the 11 dates for the image sensing time in the interferograms. Images (a)-(g) show the observed wrapped phases of the interferograms capturing the surface deformation of the seismic swarm, while no clear deformation signal is detectable in image (h). The spatial reference point is [38.3875°N, 118.725°W].

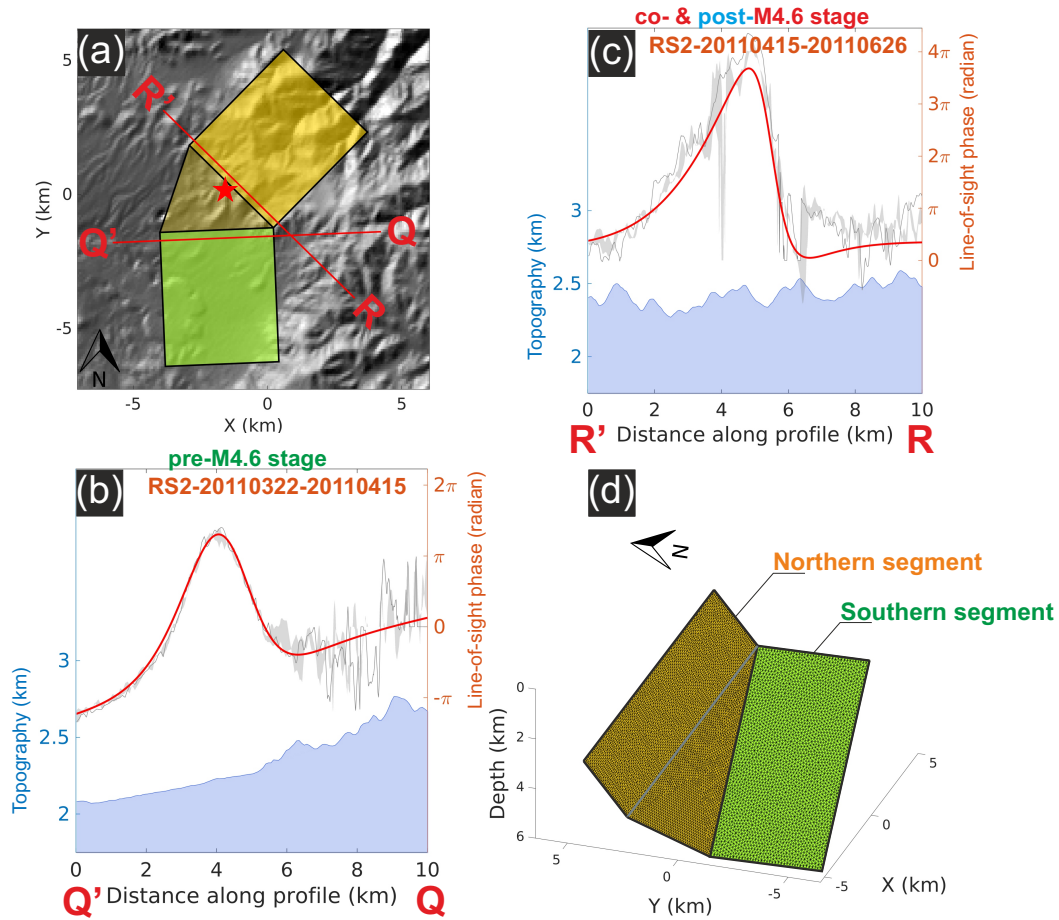


Figure 7. Fault geometry for the 2011 Hawthorne seismic swarm. Image (a) indicates the fault plane with uniform slip retrieved by WGBIS (Jiang & González, 2020) from the wrapped interferograms, and the modelled phase and phase residuals are shown in Figure S8. In image (a), the green rectangle indicates the southern subfault which is active during the pre-M4.6 stage, retrieved from RADARSAT-2 interferogram 2011/03/22-2011/04/15; yellow rectangle indicates the northern subfault which is active during the co- and post-M4.6 stages, retrieved from the RADARSAT-2 interferogram 2011/04/15-2011/06/26, and the yellow triangle indicates the joint fault connecting two rectangle subfaults. Profiles QQ' and RR' are perpendicular to two rectangle subfaults and the red star indicates the hypocentre of the M4.6 event. Images (b) and (c) show the observed and modelled phase along profiles QQ' and RR'. Image (d) shows the discretization of the fault geometry in image (a), where the triangular mesh is generated by FaultResampler (Barnhart & Lohman, 2010) and mesh2d (Engwirda, 2014).

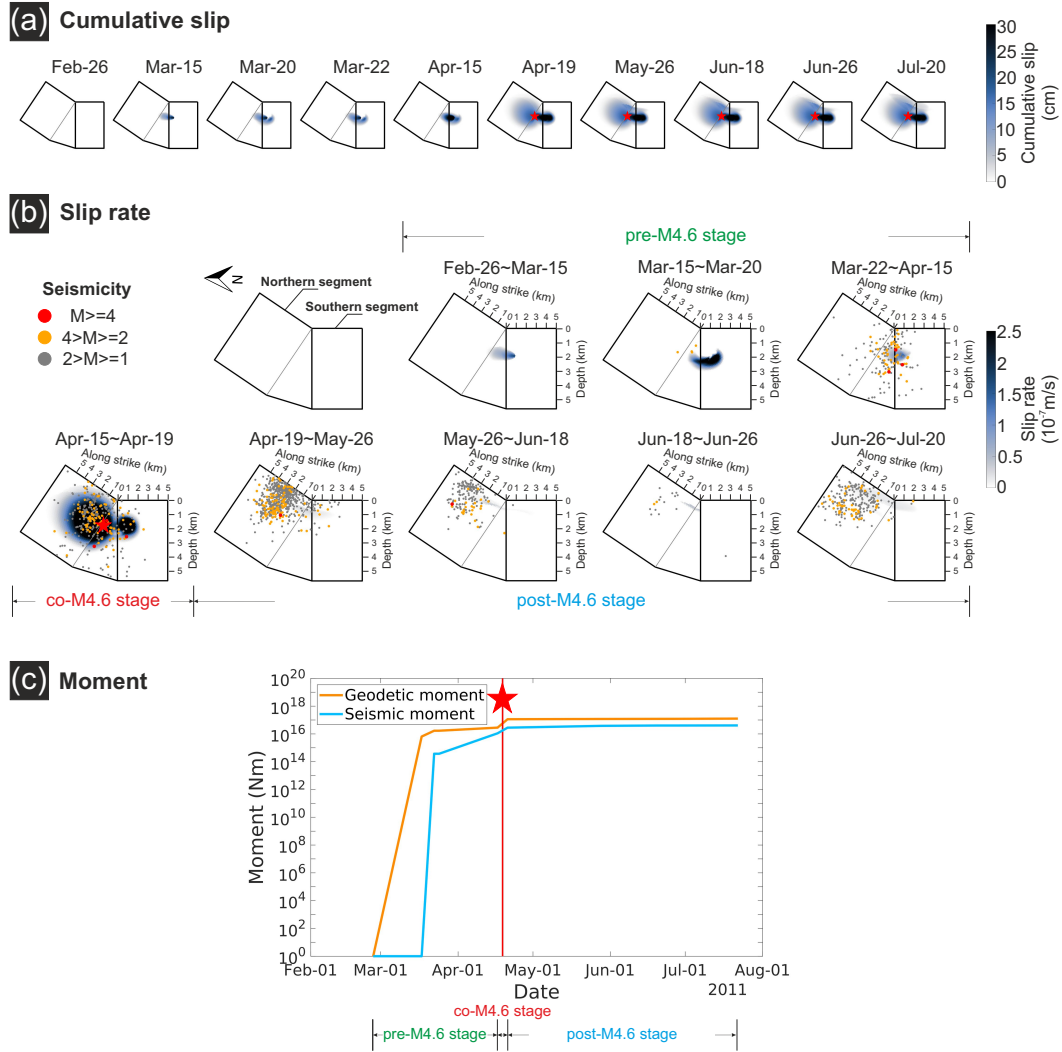


Figure 8. Slip evolution obtained from Time-GICMo inversion of pre-, co- and post-M4.6 stages during 2011 Hawthorne seismic swarm. Image (a) shows the accumulated slip at 10 dates, representing the acquisition time of images in Figures 6a to 6g. Image (b) presents the slip rate during the pre-, co- and post-M4.6 stages. In image (c), blue line shows the cumulative seismic moment based on the USGS earthquake catalog in the region [$38.325^{\circ}\text{N} \sim 38.45^{\circ}\text{N}$, $118.675^{\circ}\text{W} \sim 118.775^{\circ}\text{W}$] (<https://earthquake.usgs.gov/earthquakes/search/>); orange line shows the cumulative geodetic moment, on the basis of estimated cumulative slip in image (a). A variable crustal shear modulus with depth is assumed based on the CRUST 1.0 model in the moment calculation.